Shark biomimetics: Drag reduction beyond parallel riblets.
Transfer report

Charlie Lloyd : sccjl@leeds.ac.uk

Supervised by
Professor Jeff Peakall, Dr Alan Burns,
Dr Gareth Keevil, and Dr Robert Dorrell.

16th June 2017

Contents

1 Introduction

Dean and Bhushan (2010) define biomimicry as the study of naturally occurring properties of plants and animals for the purpose of inspired design. This particular project investigates how we can reduce the fluid dynamic drag that acts on surfaces, such as ship hulls and aircraft wings, by investigating animals that swim long distances in the ocean. There are several natural mechanisms that have evolved to reduce drag, such as the excretion of mucus, but sharks possess a unique method that can be theoretically replicated and applied to smooth surfaces (Dean and Bhushan, 2010). Sharks have evolved dermal denticles (skin teeth) which help the fish defend against parasites, abrasion, and reduce hydrodynamic drag (Fletcher et al., 2014). While the hydrodynamic benefit of shark scales has been known for decades, most work has been focussed on the riblet features that exist on the crest of some shark scales, examples of which can be observed in Figure 1. These riblets have been simplified and applied to channel flows and aerofoils, typically achieving a maximum drag reduction of $\sim 10\%$ (Discussed in Section 2).

However, riblets are one of many features that are present on shark scales (see Figure 1). Through observation of the surface it is clear that the scales are very three-dimensional and variable in geometry between different shark species and location on the shark (Fletcher, 2015). Some shark species have scales with no riblets, loosely interlocking scales, and variable angles of attack (Fletcher, 2015). It is the variability of shark scales that is the primary focus of this project. Before defining the project research question, aim, and objectives, the literature concerning riblet and shark scale experiments will be reviewed.

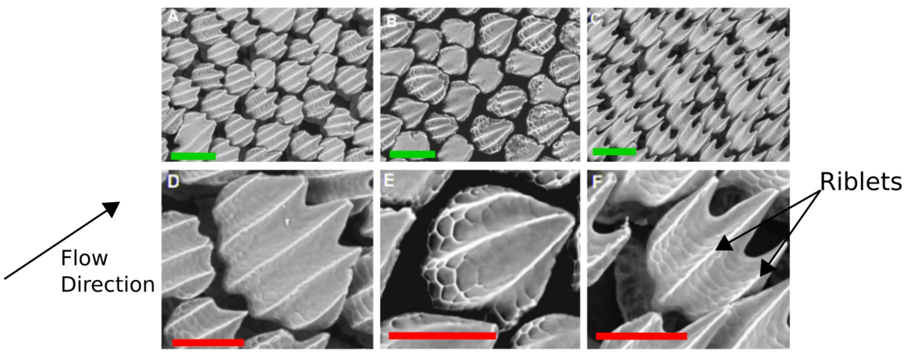

Figure 1: Shark scale samples taken from the head (A, D), the dorsal fin (B, E), and the anal fin (C, F) of a Mako shark. Green scale bars are 200 μm; red scale bars are 100 μm. Image adapted from Wen et al. (2014).

2 Literature Review

Sharks are the only surviving fishes that possess dermal denticles (Fletcher, 2015). These small tooth-like structures erupt through soft skin tissue and are optimised for the prevention of abrasion, defence against parasites, and the reduction of hydrodynamic drag (Fletcher, 2015). An extensive range of dermal denticles are documented by Reif (1985), highlighting the differences between shark species and the location of scales on the fishes. The study also indicates the complex features of real shark scales such as three dimensionality beneath the exposed scale, overlapping, diverging and converging riblets, variable angles of incidence, and the aerofoil-like shape of each scale with a smooth leading edge and a sharp trailing edge. These features can be observed in Figure 2; even when considering just one species the scales can vary significantly when moving from the head

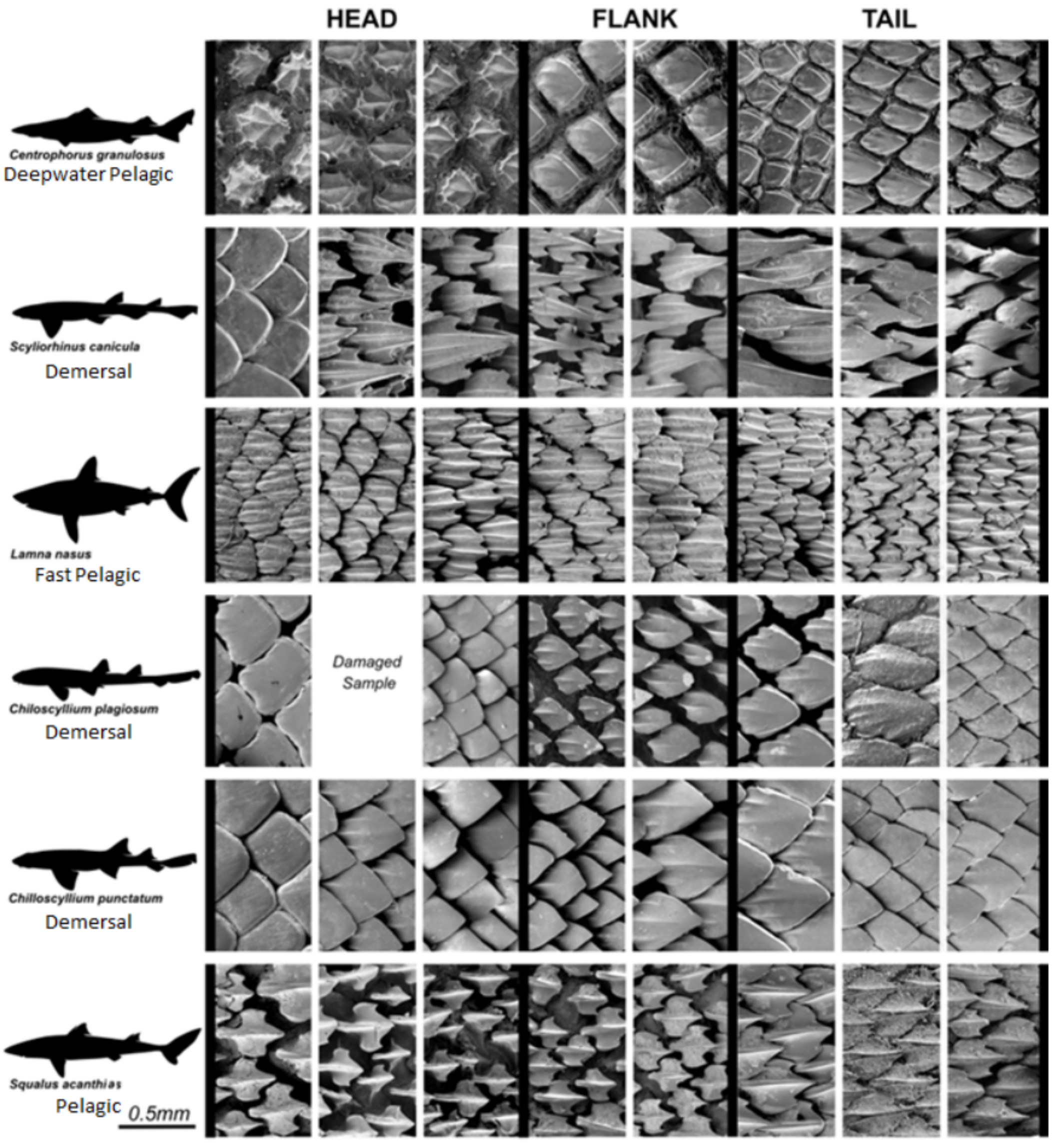

Figure 2: The variation of denticles between six fish species. Image taken from (Fletcher, 2015).

to the tail. Take, for example, the *Scyliorhinus canicula* (demersal ecology) samples in Figure 2; the scales on the head of the shark are tightly interlocking and rounded scales which quickly change to sharp, loosely interlocked, and riblettted scales on the shark's flank. The vast range of these features, and the variability between species, results in little understanding as to why many of these features exist. Hydrodynamical aspects have only been studied over the last few decades (Dean and Bhushan, 2010) and have mainly focussed on riblets, examples of which are most prominent on the fast pelagic samples of Figure 2. There has been research into the fluid dynamics of shark scales but there are many gaps and inconsistencies in the literature. These will be discussed in Section 2.4.

2.1 Boundary layers and skin friction

Most engineering and atmospheric flows are bounded by one or many surfaces. These take the form of external flows, such as the flow around cars and aircraft, and internal flows, such as through pipes and channels. Boundary layers are formed as a fluid passes over a surface, whereby the fluid velocity converges to zero as the distance to the wall decreases. Skin friction, arising from the no-slip condition, can be a large contribution to the total drag force that impedes the motion of an object: 50 % of the drag that acts on a ship hull is due to skin-friction (Perlin et al., 2016). A typical boundary layer is presented in Figure 3, which splits the temporally averaged streamwise velocity into several different regions. The velocity and spatial variables are scaled using the fluid kinematic viscosity, ν, and friction velocity, $u_\tau = \sqrt{\tau_w/\rho}$, where τ_w is the wall shear stress and ρ is the fluid

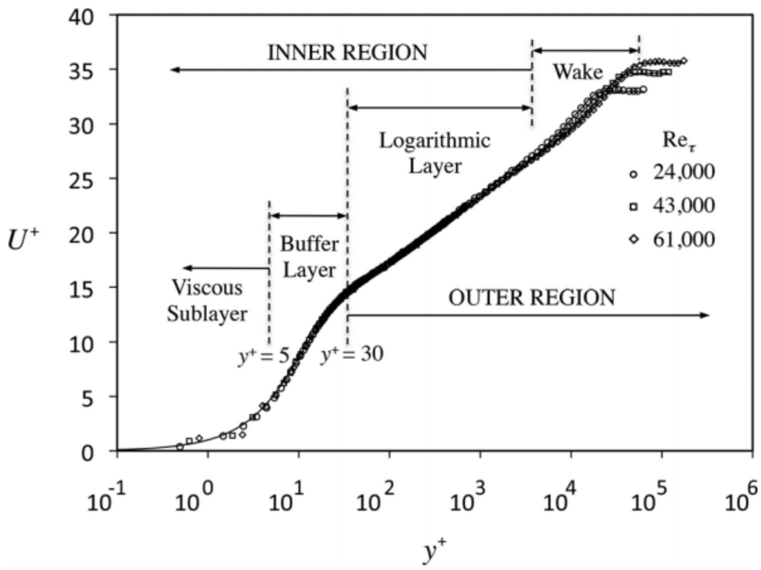

Figure 3: Typical boundary layer profile for three Reynolds numbers. Image taken from Perlin et al. (2016).

density:

$$U^+ = \frac{U}{u_\tau}, \qquad y^+ = \frac{u_\tau y}{\nu}. \tag{1}$$

By using this scaling the velocity profiles of many external and internal flows behave in the way indicated by Figure 3, whereby the boundary layer is split into external and internal regions. The inner region consists of a viscous sub-layer, a buffer layer, and a logarithmic layer. When in the viscous sub-layer the streamwise (wall-parallel) velocity of a fluid is proportional to the distance away from it, such that $U^+ = y^+$. This extends until $y^+ \approx 5$, at which point the production of turbulent kinetic energy rapidly increases until reaching its maximum in the buffer layer (Perlin et al., 2016). The logarithmic region begins at $y^+ \approx 30$, at which point the streamwise velocity behaves like $U^+ = \kappa^{-1} \ln y^+ + B$ where $\kappa \approx 0.4$ is the von Karman constant and $B \approx 5$ is the intercept parameter (Pope, 2001).

The outer layer blends the logarithmic region into the freestream velocity. The wake region, identified by Figure 3, deviates from the log-law and can cover a large amount of the boundary layer. For an external flow the wake region typically exists for $y/\delta^* > 0.2$ where δ^* is the boundary layer thickness, defined as the point at which the mean streamwise velocity is equal to 99 % of the freestream velocity, U_∞ (Pope, 2001). Surface roughness, including shark scales, has no effect on the wake portion of the outer boundary layer (Flack and Schultz, 2010).

Relationships between the skin friction drag and the flow field can be derived from the Reynolds equations (2) and the continuity equation (3) (Pope, 2001):

$$\frac{\partial \langle U_i \rangle}{\partial t} + \langle U_j \rangle \frac{\partial \langle U_i \rangle}{\partial x_j} = -\frac{\partial \langle P \rangle}{\partial x_i} + \nu \left(\frac{\partial \langle U_j \rangle}{\partial x_i} + \frac{\partial \langle U_i \rangle}{\partial x_j} \right) - \frac{\partial \langle u_i u_j \rangle}{\partial x_i}, \tag{2}$$

and

$$\frac{\partial \langle U_i \rangle}{\partial x_i} = 0, \tag{3}$$

where the three component velocity vector, U_i, and the kinematic pressure, P, are decomposed into an ensemble mean and fluctuating component: $U_i = \langle U_i \rangle + u_i$, and $P = \langle P \rangle + p$. $\langle u_i u_j \rangle$, is termed the Reynolds stresses which account for the effect of velocity fluctuations on the mean flow (Pope, 2001). The FIK identity, named after Fukagata, Iwamoto, and Kasagi, manipulates (4) to determine a relationship for the coefficient of skin friction (Fukagata et al., 2002). For a statistically steady and fully developed channel flow the FIK identity reduces to

$$C_f = \frac{\tau_w}{\frac{1}{2}\rho U_b^2} = \frac{12}{Re_b} + 12 \int_0^\delta 2\left(1 - \frac{y}{\delta}\right)\left(-\frac{\langle u_x u_y \rangle}{4U_b^2}\right) dy, \tag{4}$$

where C_f represents the coefficient of friction and Re_b is the bulk Reynolds number based on the bulk velocity, U_b, and the channel half height, δ. Similar equations can also be derived for pipe flows and flat plates. Newhall (2006) derives an integrated boundary layer equation, similar to (4), to compare the skin friction coefficients for smooth and rough flat plate flows.

By setting the Reynolds stresses to zero it is clear that (4) is decomposed into a laminar and turbulent component (Kasagi and Fukagata, 2006). It is the reduction of this turbulent component that is key to how riblets reduce drag, as will be discussed in Section 2.3.

2.2 Surface roughness

The majority of real engineering problems are subject to surface roughness which generally increases skin friction. The first quantitative study on the effect of surface roughness was carried out by Nikuradse (1933) who applied different grain sizes of sand to a pipe flow and measured the resulting friction factor (equivalent to the coefficient of friction, C_f). Nikuradse (1933) observed that for laminar, and transitional flows, surface roughness had little effect, and its effect on fully turbulent flows was dependent on the relative size of the roughness. To describe the effect of roughness on turbulent flows three regimes were defined, based on the average roughness height, k_s:

$$\frac{k_s u_\tau}{\nu} < 5 : \text{Hydraulically smooth,}$$

$$5 \leq \frac{k_s u_\tau}{\nu} \leq 70 : \text{transitionally rough,}$$

$$70 < \frac{k_s u_\tau}{\nu} : \text{fully rough.}$$

The hydraulically smooth regime occurs when the roughness elements do not protrude above the viscous sub-layer; in this case roughness has no effect. During the transitional stages roughness elements begin to protrude beyond the viscous sub layer, creating additional turbulent mixing and form drag on individual elements; both of these effects increase the friction factor relative to a smooth surface. The effect of roughness continues to grow until entering the fully-rough regime, at which point the friction factor is no longer a function of the Reynolds number.

In terms of the mean velocity profile, roughness has the effect of shifting the logarithmic layer towards the wall such that the velocity behaves like

$$U^+ = \frac{1}{\kappa} \ln y^+ + B - \Delta U^+, \tag{5}$$

where ΔU^+ represents the shift (Newhall, 2006). The gradient of the logarithmic region remains the same for both smooth and rough surfaces. In addition to this the outer layers of the boundary experience no change when subject to surface roughness, despite there being an increase to the boundary layer thickness, δ^* (Perlin et al., 2016).

2.3 Riblets

An extensive amount of work has been carried out on simplified, sharkskin-inspired, riblets which has been successful in reducing drag for open channel flows, closed channel flows, and when applied to aerofoils (Bixler and Bhushan, 2013). These riblets are generally two-dimensional, whereby there is no variation in cross section in the streamwise direction. The most popular cross sectional shapes are blade-like, sawtooth, and scalloped, although they are theorised to reduce drag in the same way. An example of blade-like riblets is presented in Figure 4, and when compared to the denticle samples of Figure 2 it is clear that the intricate details present on real shark scales are lost. Riblets are typically characterised by their spacing in wall units, $s^+ = u_\tau s/\nu$ (Dean and Bhushan, 2010), although other length scales have been suggested. For example, Garcia-Mayoral and Jimenez (2011) propose a scaling based on the cross-sectional groove area, $(A_g^+)^{1/2}$. The performance of a typical ribletted surface is presented in Figure 5, whereby the difference in wall shear stress, $\Delta\tau/\tau_0$, is plotted against the dimensionless riblet spacing, s^+. The viscous regime exists for riblets with a spacing of $s^+ \lesssim 15$ whereby the drag reduction scales linearly with spacing. For a small riblet spacing the riblets are submerged in the viscous sub-layer. Realising this, Luchini et al. (1991) used the two-dimensional linear Stokes equations to investigate the flow field. The performance of a particular riblet geometry was found to be related to its virtual origin, whereby the riblet surface can be represented by a flat plate whose origin lies somewhere below the riblet tips. Luchini et al. (1991) determined that the virtual origin of spanwise flow lies deeper in the riblet than for streamwise flow. The difference between these two origins is termed the protrusion height, Δh. Luchini et al. (1991) argued that the larger the protrusion height, the larger the restriction on spanwise flow that could otherwise lead to turbulent mixing above the riblets. This theory is supported by the inhibition of near-wall low speed streaks observed by Chu and Karniadakis (1993), and the study of Yang et al. (2016) who observed a reduced number of sweep and ejection events over a ribletted surface which are known to be large contributors to turbulent mixing (Pope, 2001).

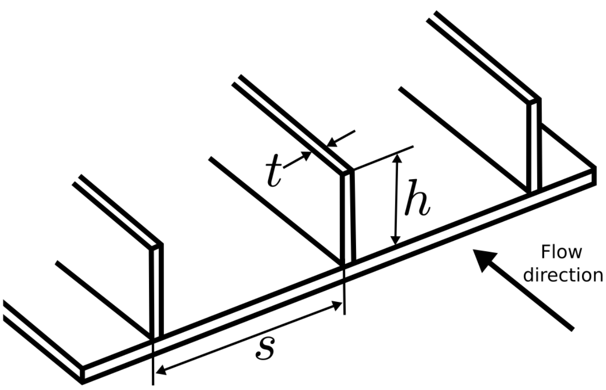

Figure 4: An example of blade-like riblets.

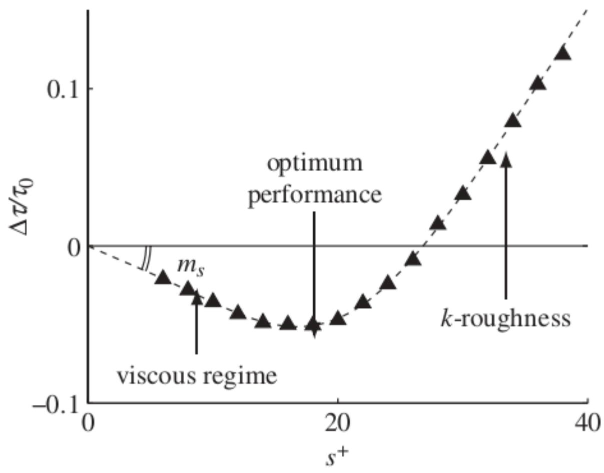

Figure 5: A typical drag reduction profile for a ribletted surface. Image taken from García-Mayoral and Jiménez (2011).

A commonly cited empirical relationship predicting the drag reduction of a ribletted surface was derived by Bechert et al. (1997):

$$\frac{\Delta\tau}{\tau_0} = m_s s^+ = -\frac{\mu_0(\Delta h/s)}{(2C_f)^{-1/2} + (2\kappa)^{-1}} s^+, \tag{6}$$

where m_s is the gradient indicated by Figure 5 and $\mu_0 = 0.785$ is an empirical constant. The roughness parameter of (5) is related to the protrusion height by $\Delta U^+ = -\mu_0 \Delta h^+$, such that the mean velocity profile is shifted away from the wall, contrary to typical rough surfaces. This theory provides a reasonable estimation for the performance of small riblet spacings; through Direct Numerical Simulation (DNS) Garcia-Mayoral and Jimenez (2011) identified a stable spanwise recirculation pattern inside the riblet spacing that mimicked those of a two-dimensional linear Stokes solution. This recirculation pattern became increasingly unstable and asymmetric as the spacing increased. At the optimal region, Garcia-Mayoral and Jimenez (2011) identified the formation of large spanwise vortices, above the riblet tips, due to a Kelvin-Helmholtz type instability. The same vortices were identified in further simulations at a Reynolds number of $Re_\tau = u_\tau\delta/\nu = 550$ (García-Mayoral and Jiménez, 2012). García-Mayoral and Jiménez (2012) also suggest that simulations at low Reynolds numbers of $Re_\tau = 180$, commonly observed in the literature, are equally valid for the study of surface roughness as higher Reynolds numbers, despite perhaps not being as representative of the flow conditions for practical applications.

As the dimensionless riblet spacing increases the riblets begin to interact with layers above the viscous sub-layer and the predictions of (6) deviate from experiments. The region after the optimum performance behaves like k-roughness, whereby the roughness parameter can be represented by $\Delta U^+ = \kappa^{-1} \ln k_s + A$, where the roughness height, k_s, is related to the dimensions of the riblet (Jimenez, 2004). As the riblet spacing increases,

Table 1: Summary of experimental literature concerning the application of riblets to open channel flows. Adapted from Bixler and Bhushan (2013).

Design	Confirguration	Material	Maximum Drag Reduction	Reference
Sawtooth	Continuous	Polymer	8%	(Reidy and Anderson, 1988)
Sawtooth	Continuous	Vinyl	9%	(Rohr et al., 1992)
Sawtooth	Continuous	Vinyl	6%	(Walsh, 1990)
Sawtooth	Continuous	Vinyl	9%	(Neumann and Dinkelacker, 1991)
Blade, Sawtooth & Scalloped	Continuous	Brass	9.9%	(Bechert et al., 1997)
Blade	Staggered & Segmented	Brass	7%	(Bechert et al., 2000)
Blade	Staggered & Segmented	Epoxy	7%	(Bechert et al., 2000)
Blade	Continuous	Titanium & Nickel	4.9%	(Büttner and Schulz, 2011)
Sawtooth	Continuous	Polyurethane	7.6%	(Grüneberger and Hage, 2011)
Blade	Continuous	Metal & Polymer	8.5%	(Wilkinson and Lazos, 1988)
Sawtooth, Scalloped	Continuous	Aluminium & Vinyl	8%	(Walsh, 1982)

they lose their ability to constrict spanwise flow and fast moving fluid can penetrate to the base of the grooves, as observed by Lee and Lee (2001).

The application of riblets to adverse pressure gradients (APG) is still an area of much uncertainty (Boomsma, 2015). Tables 1 and 2 indicate the discrepancies between the application of riblets to channel flows and aerofoils. Even when taking into account the different configurations and riblet types, open channel flow experiments indicate a range of only 5 % for the maximum drag reduction. When riblets are applied to aerofoils the range increases to 10 %. This is largely due to the additional dependencies on riblet configuration and the shape of the foil; the experiments of Chamorro et al. (2013), carried out on a wind turbine blade, indicate that for some cases a partially ribletted foil reduces drag more than a fully covered foil. This is due to development of the boundary layer over the foil; unlike the fully turbulent channel flow experiments the boundary layer of an aerofoil transitions from laminar to turbulent. Uncertainty is further introduced by

Table 2: Summary of experimental literature concerning the application of riblets on aerofoils. Adapted from Bixler and Bhushan (2013).

Foil Type	Location of Trip (% Chord Length)	Angle of Attack (degrees)	Maximum Drag Reduction	Reference
Symmetric, Thin	No Trip	0	4.3%	Han et al. (2003)
Symmetric, Thin	No Trip	0	13.3%	Caram and Ahmed (1991)
Thin	10%	0-6	6%	Sundaram et al. (1999)
Symmetric	10%	0-6	13%	Sundaram et al. (1996)
Thin	5%	0	14%	Subaschandar et al. (1999)
Thick	No Trip	0	5%	Wetzel and Farokhi (1996)
Thick	No Trip	0	5%	Sareen et al. (2011)
Thick	6%	-0.5-1	10%	Viswanath and Mukund (1995)
Thin	No Trip	0	3.3%	Coustols and Schmitt (1990)
Symmetric, Thin	5%	0	7%	Bixler and Bhushan (2013)

Table 3: Summary of experimental and numerical work concerning the drag reduction properties of shark skin

Scale Type	Replication Method	Experimental Technique	Max Drag Reduction	References
Mako, AOA 10 deg	Printing/casting	Wind tunnel + balance	-13%	Bechert et al. (1985)
Mako, AOA 5 deg	Printing/casting	Wind tunnel + balance	-4%	Bechert et al. (1985)
Silky Shark	Printing/casting	Wind tunnel + balance	-1%	Bechert et al. (1985)
Lophosteus	3D printing	Water flume + LDA	35%*	Fletcher (2015)
Carcharhinus Brachyurous	Moulding	Water flume + balance	12%	Chen et al. (2014)
Not reported	Moulding	Water flume + balance	18.6%	Zhao et al. (2012)
Isurus Oxyrinchus	Moulding	Water flume + balance	8%	Zhang et al. (2011a)
Isurus Oxyrinchus + polymer	Moulding	Water flume + balance	24%	Zhang et al. (2011a)
Not reported	Moulding	Water flume + balance	12%	Luo et al. (2015b)
Carcharhinus leucas	Moulding	Water flume + balance	12%	Luo et al. (2015a)
Carcharhinus leucas + stretched	Moulding	Water flume + balance	14%	Luo et al. (2015a)
Mako	3D printed	Water flume + balance	8.7%	Wen et al. (2014)
Mako	3D printed	Water flume + balance	10%	Wen et al. (2015)
Not reported	Scanned + smoothed	Numerical RANS	13%	Zhang et al. (2011b)
Not reported	Moulding	Water flume + balance	9.5%	Zhang et al. (2011b)
Mako	Scanned + smoothed	Numerical DNS	-50%*	Boomsma (2015)

some experiments using a boundary layer trip to shift the transitional point towards the leading edge (see Table 2). There have been more fundamental approaches to the investigation of riblets applied to APG flows; Choi (1990) use a wind tunnel with an adjustable wall height to vary the pressure gradient. It is concluded that the reduction of skin friction is independent of the pressure gradient. In contrast, Nieuwstadt et al. (1993) and Debisschop and Nieuwstadt (1996) indicate a drag reduction twice the magnitude of a zero pressure gradient (ZPG) case for an APG case. This is achieved by applying riblets to a diffuser. These results are further supported by the LES of Klumpp et al. (2010) and Boomsma (2015). However, little reasoning behind this increase is given; Boomsma (2015) does provide evidence that the drag reducing mechanisms are the same for both ZPG and APG flows but fails to answer why riblets in an APG are more effective.

2.4 Investigations of the fluid dynamics of shark scales

There have been very few hydrodynamic experiments carried out on shark scales, and those that have been carried out are rarely in agreement. Table 3 summarises the hydrodynamic experiments that have been carried out on shark scale surfaces applied to channel flows and flat plates. The maximum drag reduction ranges from an increased drag of 50 % to a decreased drag of 35 %. It should be noted that these extreme cases (highlighted with an asterisk in Table 3) were only carried out at a single flow rate unlike the other studies. Thus they are limited to a single calculation of the drag force. The drag reduction of 35 % is associated with the work of Fletcher (2015) who adopted Laser Doppler Anemometry to measure the coefficient of drag for 5 different arrays of fish scales. The scales were 3D printed to a normalised scale length of 2 mm, ensuring that the denticle features were captured to an appropriate resolution. However, no attempt was made to non-dimensionalise the scale width, as opposed to comparable studies on riblets. The use of LDA in this particular case is also questionable: Newhall (2006) validates the use of flow field measurements to calculate the coefficient of drag but suggests that the most accurate method is to measure drag directly, such as through the use of force balances. The advantage of LDA is that flow fields can be resolved such as the Reynolds stresses but only the mean velocity profiles are reported by Fletcher (2015). Comparable studies by Wen et al. (2014, 2015) were carried out using mako scales printed at a width of 1.6 mm. The scales in question had riblets on the denticle crown, the spacing of which was used to determine an s^+ value for each flow rate. Drag was directly measured using a force balance and the profile of Figure 6 was obtained. In this case, the difference in drag was quantified by D_s/D_0 rather than $\Delta\tau/\tau_0$, where D_s and D_0 are the drag forces acting on the scales and the reference flat plate respectively. The experiments of Fletcher (2015) were carried out at a bulk velocity of ∼0.5 m/s. Figure 6 suggests that the drag reducing cases of Fletcher (2015) should be increasing drag by ∼15 % if the scales behave like those of Wen et al. (2014). It is interesting to note the profiles of Figure 6 when compared to those of the riblets in Figure 5; if the results of Wen et al. (2014) are accurate then the viscous region observed for engineered riblets does not apply to shark scales. Two questions arise from this; how does the drag reduction behave as the riblet spacing reduces further? And is there perhaps a more appropriate length scale other than the riblet spacing? Figure 7 highlights the key dimensions of the mako scale used by Wen et al. (2014). Clearly there are many other length scales that quantify a shark

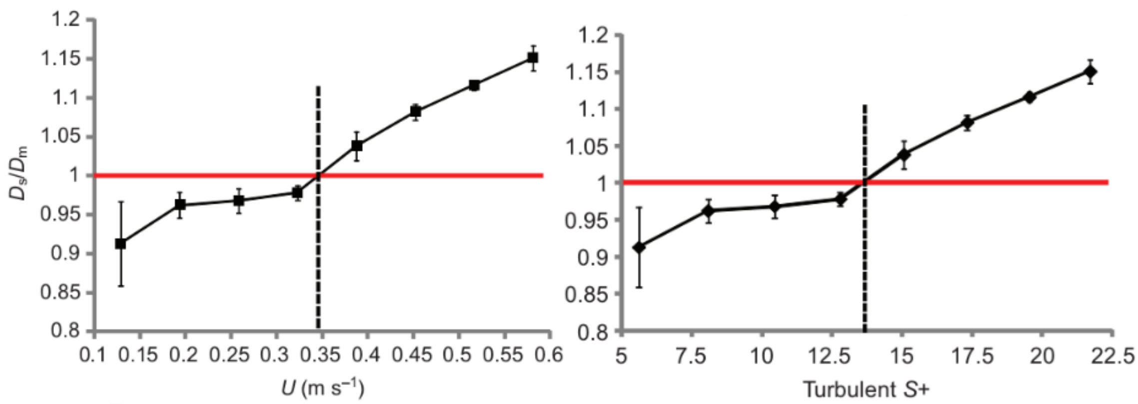

Figure 6: The drag reduction of a denticle array in terms of bulk velocity (left) and dimensionless riblet width (right). Image taken from Wen et al. (2014).

scale. The results of Wen et al. (2014) are further supported by Wen et al. (2015) when investigating the effects of denticle arrangements. Closely interlocked/overlapping scales are found to behave in the way indicated by Figure 6. In contrast, loosely interlocking scales reduce drag for $s^+ \approx 16$ by 3 % but increase drag for all over riblet spacings. It might be expected that the optimal riblet spacing for engineered riblets and shark scales would coincide for tightly interlocking scales but these results suggest otherwise. A major limitation noted by Wen et al. (2014) is the pump range of the flume which was unable to operate below a bulk flow velocity of ∼0.13 m/s. This was also the cause of the large error bars associated with the lowest flow rate, observed in Figure 6. The experiments of Bechert et al. (1985) determined an increased drag, for both mako and silky shark scales, for the full range of s^+ values. However, they did not produce results for $s^+ < 10$ which further supports the argument that smaller denticle riblet spacings need further investigation.

The other extreme result of Table 3 is the DNS of Boomsma (2015). This work adopts an immersed boundary technique to model the flow around the same denticles (staggered and aligned) printed by Wen et al. (2014, 2015), and some engineered riblets. Periodic boundary conditions are adopted to simulate a fully developed channel flow at a Reynolds number of $Re_\tau = 180$ and a riblet spacing of $s^+ = 16$ (for both the engineered riblets and the denticles). The riblet surface behaved as expected; a drag reduction of ∼5 % was predicted, arising from the reduction of the Reynolds stresses. In contrast, the denticles were found to induce separation and large vortices near the scale surface; both of which contribute to increased Reynolds stresses. The results are validated against those of Bechert et al. (1985) but over predict the drag compared to Wen et al. (2014,

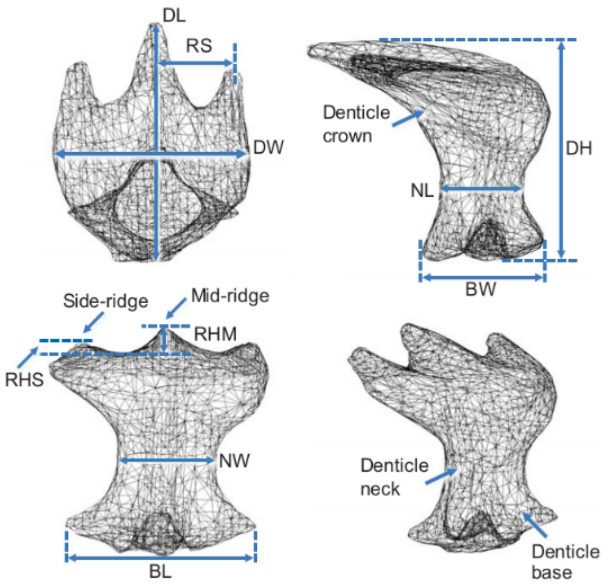

Label		Dimension
DL,	denticle length	151 μm
DW,	denticle width	125 μm
DH,	denticle height	113 μm
NL,	neck length	45.1 μm
BW,	base width	119 μm
BL,	base length	83.8 μm
RS,	riblet spacing	51 μm
RHM,	riblet height (mid)	21 μm
RHS,	riblet height (side)	11 μm

Figure 7: Micro-CT surface mesh of a mako denticle (prior to smoothing and scaling) (left) with corresponding dimensions (right). Image taken from Wen et al. (2014).

2015), despite the shark scales being identical. Boomsma and Sotiropoulos (2016) argue that this is due to the different experimental conditions of Wen et al. (2014) and Bechert et al. (1985). The denticles of Wen et al. (2014) were exposed to a developing flow, at a much higher Reynolds number than the simulations. However, the DNS of García-Mayoral and Jiménez (2012) suggests that, for riblet surfaces, low Reynolds number flows are comparable to high Reynolds number flows, as long as the s^+ values are identical. Boomsma and Sotiropoulos (2016) provide no reason as to why the experiments of Bechert et al. (1985) are in agreement with theirs.

Referring to Table 3 there is still a large spread of drag reduction results, even when ignoring the two extremes. Generally the maximum drag reduction of shark scales is of a greater magnitude than those of engineered riblets, contrary to the results of Bechert et al. (1985). Chen et al. (2014) observes similar drag reduction behaviour for both engineered riblets and ribletted denticles. The denticles consistently outperformed the riblets for the full range of flow rates, achieving a maximum reduction of 12 %. However, there is no effort made to relate the bulk velocity to a dimensionless parameter such as s^+. The denticles were fabricated using a mould which was created from a real shark scale surface. The authors report a replication error of only 2 % but there are several issues with this technique that are not discussed. Imperfections, asymmetries, and changes in denticle geometry that exist on real shark scale arrays are all captured using the moulding technique. Clearly this model is more physical, but isolating the effects of slight geometric changes between the different denticles is unrealistic using current experimental methods. To the author's knowledge, only tightly interlocking scales have been replicated using this technique (Zhang et al., 2011b,a; Zhao et al., 2012; Chen et al., 2014; Luo et al., 2015a,b). It has yet to be established whether the same methods can be applied to more loosely interlocking scales which are equally common among different shark species (see Figure 2).

A similar technique is adopted by Zhao et al. (2012); a drag reduction of 18% is achieved at the lowest velocity measured, which then reduces to a local minimum, raising to a local maximum and then reduces to its minimum value at the highest fluid velocity. This result is not discussed, and without support from other literature the validity of the experimental techniques is questionable. Zhang et al. (2011a) adopts the same moulding technology on a *Isurus oxyrinchus* sample. Drag reduction is compared for a ribletted surface, sharkskin replica and a sharkskin replica with non-long polymer chains attached to the surface. The polymer surface was introduced as a method to mimic the mucus excretion of sharks. Small fishes are known to rely on mucus excretion to increase burst swimming speeds; when added to a fluid this mucus can reduce drag by up to 66 % (Fletcher, 2015). However, unlike most fishes, sharks mucus production is restricted to small areas below the denticle crowns. It is therefore often assumed that mucus excretion has a lesser effect for sharks although the topic is still poorly understood (Fletcher, 2015). Zhang et al. (2011a) measures a maximum drag reduction of 8 % for the sharkskin replica which increases to 24 % when the polymer is added. In addition to this, the drag reduction effect increases with increasing flow rate, contrary to the sharkskin without polymer added to its surface. However, Fletcher (2015) suggests that mucus is excreted from pores below the scales. Zhang et al. (2011a) applies the polymer coating to the whole surface which is perhaps not a physical representation of mucus excretion.

Zhang et al. (2011b) adopts numerical and experimental techniques to investigate the drag reduction of moulded shark scales, although little detail is presented explaining either of the adopted methods. The experimental results indicate a maximum drag reduction of 12.8 % at the slowest flow rate which then asymptotes to a value of ∼9 %. This behaviour is similar to that of the non-polymer covered sharkskin of Zhang et al. (2011a), although the magnitude of drag reduction is consistently ∼3 % higher. The numerical simulations of Zhang et al. (2011b) adopt a finite volume method, with a $k - \epsilon$ turbulence closure, to solve the developing flow field over an array of ∼30 shark scales. The shark scales were micro-CT scans of those that were replicated. While the model predicts a drag reduction of the same order as the experiments they increase from 7 % to 14 % as the flow rate increases; i.e a trend opposite to the experiments. There are several potential causes, such as a lack of grid dependence, convergence, and the use of $k - \epsilon$, which is known to perform poorly in boundary layers (Pope, 2001). However, none of these issues are discussed by Zhang et al. (2011b). Despite this these results are often used to justify the drag reduction observed in experiments (Zhao et al., 2012; Chen et al., 2014).

This section has so far only discussed the literature associated with shark skin applied to flat plates and channel flows. These simple flow configurations are commonly adopted due to their applicability to a wide range of engineering flows, and the repeatability of experiments. This is made clear when referring to the riblet experiments of Section 2.3; channel flows and flat plate experiments agree more closely than when riblets are applied to aerofoils. However, the flow field around a shark is far from the idealised flow in channels. Díez et al. (2015) attempts to resolve the flow around a shortfin mako shark using Computational Fluid Dynamics (CFD). The model adopts the $k - \epsilon$ turbulence closure with wall functions to reduce computing costs. In addition to this, a roughness parameter is used to account for the denticle surface. This is clearly a large simplification to the shark scale geometry but the general flow field around the shark body is captured. The coefficient of drag as a function of position is presented in Figure 8. The results of Díez et al. (2015) indicate a spike in the coefficient of drag near each of the fins and a slowly decreasing coefficient of drag along the main body. The authors also investigated scale morphology, whereby 24 SEM images were taken at various locations on the shark body, although little analysis is provided linking the morphology to the CFD flow field. The authors do note that smooth scales typically exist on the leading edge of the fins and the nose of the shark. Riblets are found to be introduced further downstream. One could

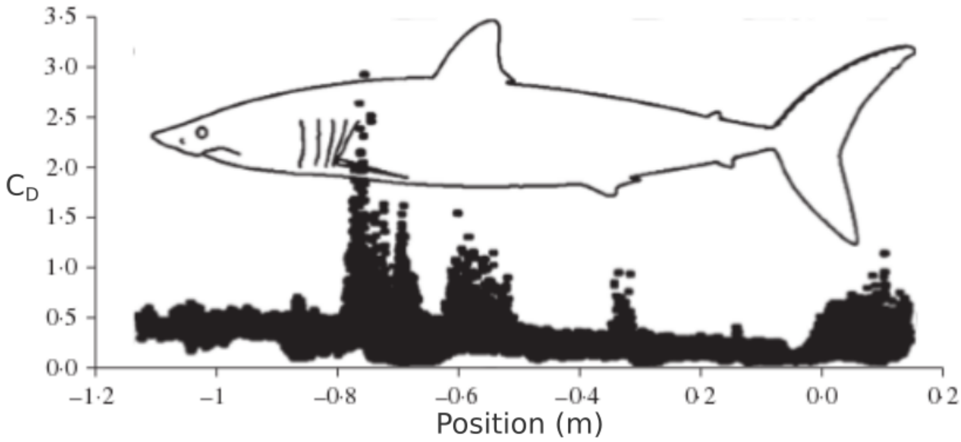

Figure 8: The coefficient of drag distribution over a mako shark. Image taken from Díez et al. (2015).

postulate that since a boundary layer develops from laminar to turbulent, and knowing that surface roughness has no effect in laminar flows (see Section 2.2), the transition from smooth scales to ribletted scales reflects the transition from a laminar to a turbulent boundary layer. However, the same conclusion cannot be drawn when considering the morphological study of Fletcher (2015). Figure 9 displays the contour maps of two denticle geometries over the body of a Lamna nasus (Fletcher, 2015). Strongly converging riblets can be observed on the nose and pectoral fin of the fish and slightly converging scales are found on the dorsal fin. Fletcher (2015) hypothesises that converging riblets could

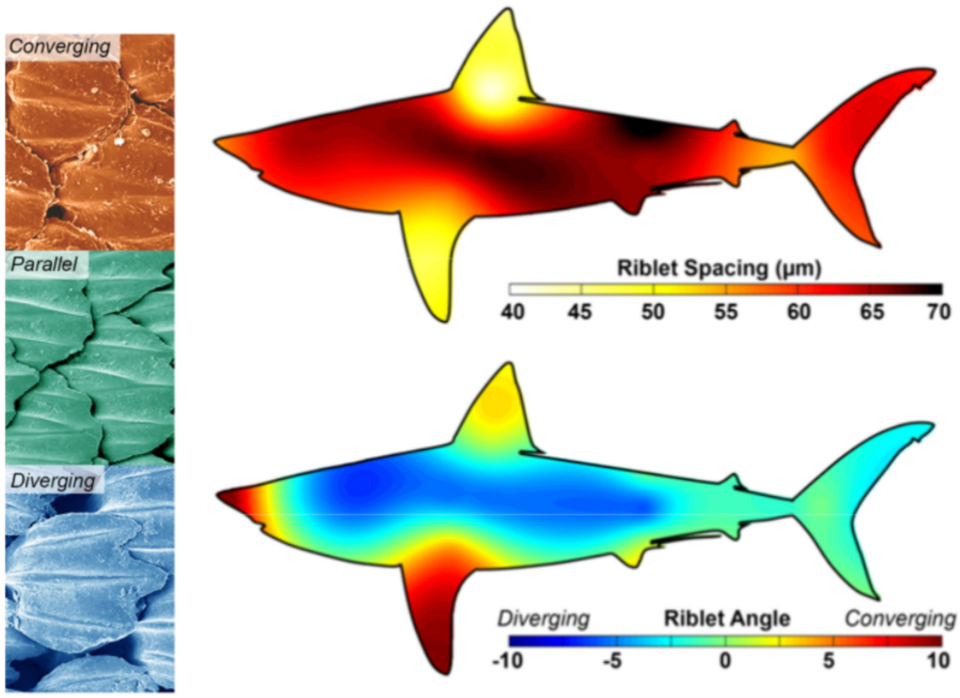

Figure 9: Distributions of riblet spacing and riblet angle for a Lamna nasus. Image taken from Fletcher (2015).

act as a turbulent trip, similar to those observed on aerofoils (see Section 2.3). This is further supported by the conclusions of Bechert et al. (1985) who argue that denticles could increase turbulent mixing and result in a reduced susceptibility to flow separation. If this is the case then why does the mako shark analysed by Díez et al. (2015) possess smooth scales on the nose? Figure 9 also indicates reduced riblet spacing on the fins. Referring to Section 2.3 small riblet spacings are associated with higher flow rates; i.e an increase to the friction velocity, u_τ will require a reduction in riblet spacing, s, if the s^+ value is to be maintained. The findings of Díez et al. (2015) reinforce this by determining an increased flow velocity near the fins of the shark.

An aspect of shark skin that has not yet been discussed is the effect of passive bristling as a mechanism for maintaining attached boundary layers. This effect can be observed in Figure 10; while shark scales are rigid, they are embedded into a flexible epidermis which allows the denticle angle of attack to be altered (Lang et al., 2014). The precise mechanism that leads to this bristling is still unknown. Bechert et al. (1985) suggested that the variation in mechanical tension of the epidermis could control the bristling mechanism. At high speeds the epidermis is under larger tension than lower speeds, and perhaps it is this mechanism that drives scale bristling. However, Lang et al. (2014) concluded that the presence of recirculating flow could be enough to bristle scales alone. This is determined by imaging the effect of a small pulsating jet which created a backflow over a shark skin sample. However, the authors note that since experiments are carried out on a small section of shark skin the mechanical tension will not be matched for a real shark. Lang et al. (2014) apply these sharkskin sections to a NACA 4412 aerofoil and measure the resulting flow field using Digital Particle Image Velocimetry (DPIV). They compare the resulting backflow for a sharkskin surface with bristling scales, and a smooth surface. They find that at low angles of attack the sharkskin surface produces more backflow than the smooth surface. However, backflow is substantially reduced for large angles of attack; at a foil angle of 18° there is a large amount of separation for the smooth surface but very

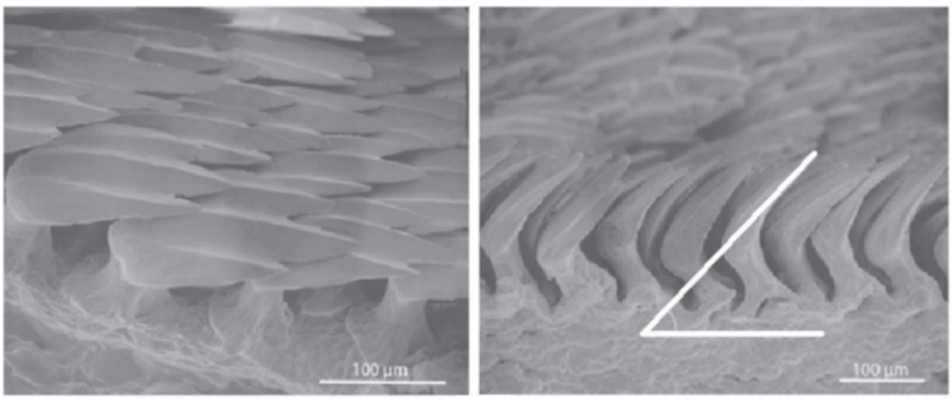

Figure 10: Bristling scales of a shortfin mako. The scales are bristled to an angle of 45°. Image taken from Lang et al. (2014).

little for the sharkskin. The authors hypothesise that at low angles of attack the backflow is too weak to induce bristling, and as a result the performance of the foil is hindered by its increased thickness. However, DPIV is unable to capture the bristling behaviour directly since the scales are so small. There are also other issues with this technique; since sharkskin is directly applied to the foil there is much uncertainty concerning the mechanical properties of the epidermis and the variability between individual scales. These issues are eliminated by the experimental technique of Wen et al. (2014, 2015) who 3D print an array of smoothed mako scales onto a flexible membrane, mimicking that of a shark epidermis. The membranes are subsequently applied to the surface of a flapping NACA aerofoil, hypothesising that the flexibility of the scales could have implications on thrust generation. Both studies conclude that the swimming speed of the flapping foil is increased when denticles are present but both the cost of transport (energy required per unit distance) and power required increased. The authors suggest that this is likely due to the poor representation of the flexible membrane to real shark skin where scales are more flexibly embedded into the dermis. It is suggested that dynamic experiments are more representative of shark skin and should be further investigated.

2.5 Summary

This section has reviewed the literature concerning engineered riblets and the experiments concerning shark scales. Several inconsistencies and gaps in the literature can be identified:

- The application of engineered riblets to flat plates and channel flows has been well studied in the literature. However, there are still inconsistencies concerning their application to adverse and favourable pressure gradients.
- There is substantial controversy between the literature associated with the application of shark scales to flat plates and channel flows. This is due to the different experimental techniques, manufacturing methods, denticle geometries, and denticle arrangements.
- While the s^+ scaling is appropriate for riblets, there are many denticle length scales that could also be considered; perhaps a combination of these would be more appropriate when considering the performance of denticles.
- Current experiments on denticles have been unable to investigate the effects of small values of s^+ on a flow. Experiments of Bechert et al. (1985) and Wen et al. (2014, 2015) indicate that drag reduction occurs for denticles at a lower s^+ value than for engineered riblets.
- Most hydrodynamic experiments have considered denticles with riblets, but there are many shark species that possess denticles without riblets. The experiments of

Fletcher (2015) suggest there could be a hydrodynamic benefit to denticles without riblets. there are also many other geometrical features that have yet to be investigated, such as the effects of converging/diverging riblets on a flow.

- Some of the most informative studies concerning engineered riblets have adopted numerical methods to investigate the intricate flow fields. Numerical techniques have the advantage of being able to provide insight into how denticles interact with a flow, but only a single DNS paper has been published in this subject area.
- The application of scales to separating flows and adverse pressure gradients has seen little investigation. Studies that have been carried out in this area have focused on large scale fluid structures rather than investigating how the flow interacts with the denticles.
- Dynamic experiments have also been recently introduced whereby the interactions between the flexible epidermis and the denticles are investigated. These methods can create more physical models but are currently limited to the observation of large scale structures.
- Mucus excretion is another subject that has seen little investigation in terms of shark skin. Authors have often disregarded its effect but the work of Zhang et al. (2011a) suggests it could have much larger implications.

3 Research questions

Section 2 indicated several gaps in the literature concerning shark scales. As a result, several research questions have been proposed:

1. What are the effects of small denticles on a flow? Does a viscous regime exist whereby scales behave like riblets?
2. Is there a more appropriate length scale, other than s^+, that can better parametrise a denticle?
3. What are the effects of denticle geometry on a flow, such as smooth scales, converging/diverging riblets, and the crowns angle of attack?
4. What are the effects of denticles on the flow field? Experiments to date have mainly adopted force balances, which cannot answer this question.
5. What are the effects of denticles on separating flows?

These questions will be answered using a mixture of experimental and numerical techniques. Questions related to denticle geometry will be answered via LDA experiments, LES, and RANS simulations. The LDA experiments will measure the effects of smooth, and ribletted, 3D printed denticles on a flat plate. LES will be adopted to investigate the effect of these denticles in a periodic channel flow, and RANS will be used to carry out a parametric analysis. There are advantages and disadvantages associated with each of these methods; LDA is a highly accurate, and non-intrusive, experimental technique, but the flow field surrounding individual scales cannot be captured. On the contrary, LES has the capabilities to resolve the turbulent structures near the scales, but requires too much computing power to carry out lots of different case studies. RANS is more suitable for parameter studies, but requires validation.

In addition to this the project will investigate the effect of applying scales to surfaces subject to separating flows. LES, or RANS, will be applied to a separating flow problem in order to quantify the differences between smooth and shark-skin surfaces. The results will be validated against a laboratory experiment using Particle Image Velocimetry (PIV).

4 Aims and Objectives

There are two aims of this project; to investigate the influence of shark scale geometry on a fully developed flow, and to investigate the impact of scales on separating flows. Both of these aims will primarily concern the flow fields close to/around the scales. These will be achieved through completion of the following objectives:

- Carry out LDA experiments for an array of scales on a flat plate, and compare against the results of a smooth surface.
- Carry out a high resolution LES for the same array of scales and validate against LDA data.
- Validate a parametric RANS code against the LES/LDA data and carry out a parametric analysis on the effect of scale geometry on the fluid flow.
- Design and carry out laboratory (PIV) and numerical experiments (TBC) that can be used to investigate the influence of shark scales on separating flows.

5 Channel Flow Experiments using Laser Doppler Anemometry

As discussed in Section 2, little work has been carried out in analysing the fluid flow around shark scale surfaces; most work has primarily made use of force balances which cannot measure velocity or pressure fields. While previous experiments have successfully measured drag reduction for sharkskin they have not yet investigated the fluid dynamic features that are causing it. For this reason we choose to adopt Laser Doppler Anemometry (LDA) to measure a channel flow, with and without shark scales. While a channel flow does not replicate the complex flow fields around a shark, it allows comparison against a wide range of empirical and numerical literature data (in the case of smooth channels), and also ensures the results are applicable to a wide range of surface flows, such as boat hulls and pipe walls. In addition to this, understanding how shark scales behave in simple and controllable configurations will provide comparative data when investigating their effects on separating flows. This simplification also allows numerical models to exploit the periodicity of shark scale surfaces, greatly reducing the required computing power for numerical methods. This section details the preliminary experiments, the aim of which is to validate the experimental method and identify changes that must be made to future designs.

5.1 Fundamentals of LDA

LDA is a non-intrusive method of determining a fluids velocity by measuring the Doppler shift of laser light (Zhang, 2010). There are several key components which can be split into two groups; an optical unit, and a receiving unit. The optical unit generates and transmits a pair of laser beams for each velocity component and focusses them onto a small volume. The two beams create a fringe pattern in the measurement volume, the spacing of which, Δx, is determined by the angle of intersection, α, and the light wavelength, λ. This is demonstrated in Figure 11, whereby a particle of velocity $\overrightarrow{u}_p$, passes through the fringe pattern created by the two beams E_a and E_b. The two beams can be represented by

$$E_a = E_0 \cos\left[\omega_a t - k_a(z\cos\alpha - x\sin\alpha)\right], \tag{7}$$

and

$$E_b = E_0 \cos\left[\omega_b t - k_b(z\cos\alpha + x\sin\alpha)\right], \tag{8}$$

where E_0 represents the wave amplitude, ω represents the respective angular frequencies, and $k = 2\pi/\lambda$ represents the angular wavenumber. The wavelength is related to the speed of light by $c = \lambda f$, where c represents the speed of light, and f represents the

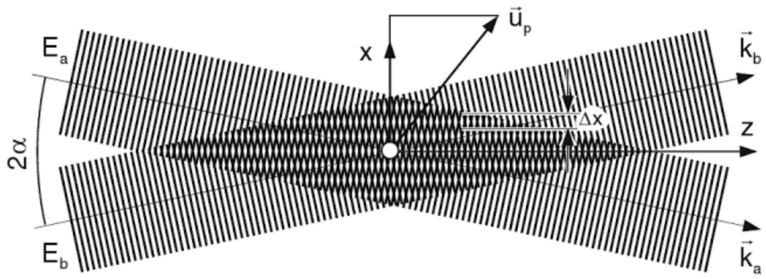

Figure 11: Fringe pattern of an intersecting pair of laser beams. Image taken from Zhang (2010).

oscillation frequency. With some manipulation the x-component of the particle velocity is found to be directly related to the fringe spacing, and the shift in oscillation frequency as the particle passes through the fringes (Zhang, 2010). The receiving components detect this change in frequency and converts this to an electrical signal which can be processed. In order to relate the particle velocity to the fluid velocity the flow is seeded with neutrally buoyant particles. It is assumed that these particles do not deviate from the fluid streamlines.

The present work makes use of two-component LDA, whereby two pairs of beams, one at $\lambda = 514.51\,\mathrm{nm}$ (green light) and one at $\lambda = 488\,\mathrm{nm}$ (blue light), are transmitted perpendicular to each other. The respective shifts in frequency are separated by the receiving unit in order to produce two velocity components. Particle velocities are only recorded if a shift in frequency is observed by both beam pairs, thus the covariance of the two velocities (Reynolds stresses) can be analysed.

Velocity biasing is a phenomena that must be considered when utilising LDA. Since velocities are only sampled when particles pass through the focal volume, the subsequent time series does not have a regular sampling interval. For this reason, high velocity fluctuations are measured more often than low velocity fluctuations, which results in a bias towards higher velocities when calculating statistics. The correction method detailed by Zhang (2010) is adopted in the present work, whereby the means and standard deviations are normalised by the amount of time a particle resides in the focal volume, τ. The temporal mean of a velocity component u is therefore calculated by

$$\mu_u = \frac{\sum_{i=1}^{N} u_i \tau_i}{\sum_{i=1}^{N} \tau_i}, \tag{9}$$

the standard deviation is calculated by

$$\sigma_u^2 = \frac{\sum_{i=1}^{N} \tau_i (u_i - \mu_u)^2}{\sum_{i=1}^{N} \tau_i}, \tag{10}$$

and the covariance between the two components of velocity is calculated by

$$\gamma_{u,v} = \frac{\sum_{i=1}^{N} \tau_i (u_i - \mu_u)(v_i - \mu_v)}{\sum_{i=1}^{N} \tau_i}. \tag{11}$$

5.2 Experimental set up

The experiments are carried out using a flat plate submerged in a recirculating flume (observed in Figure 12). The plate has the dimensions $L \times w \times h = 500 \times 100 \times 10$ (mm), with semi-circular leading and trailing edge cross sections. The volumetric flow rate is controlled by setting the pump frequency. Relating this to a Reynolds number prior to experiments is non-trivial due to the unknown bulk velocity in-between the plate and the flume wall. Subsequently, the Reynolds number is estimated from the measured profiles. The operating range of the pump is 4 Hz to 16 Hz. As discussed in Section 2.4, previous experiments have been unable to capture the effects of sharkskin at small values of s^+. Experiments are therefore carried out at low pump frequencies of 4 Hz and 8 Hz. A grid is created in order to define the locations at which the velocity is measured. The LDA probe is mounted to a traverse and calibrated such that $(0, 0, 0)$ lies along the centre of

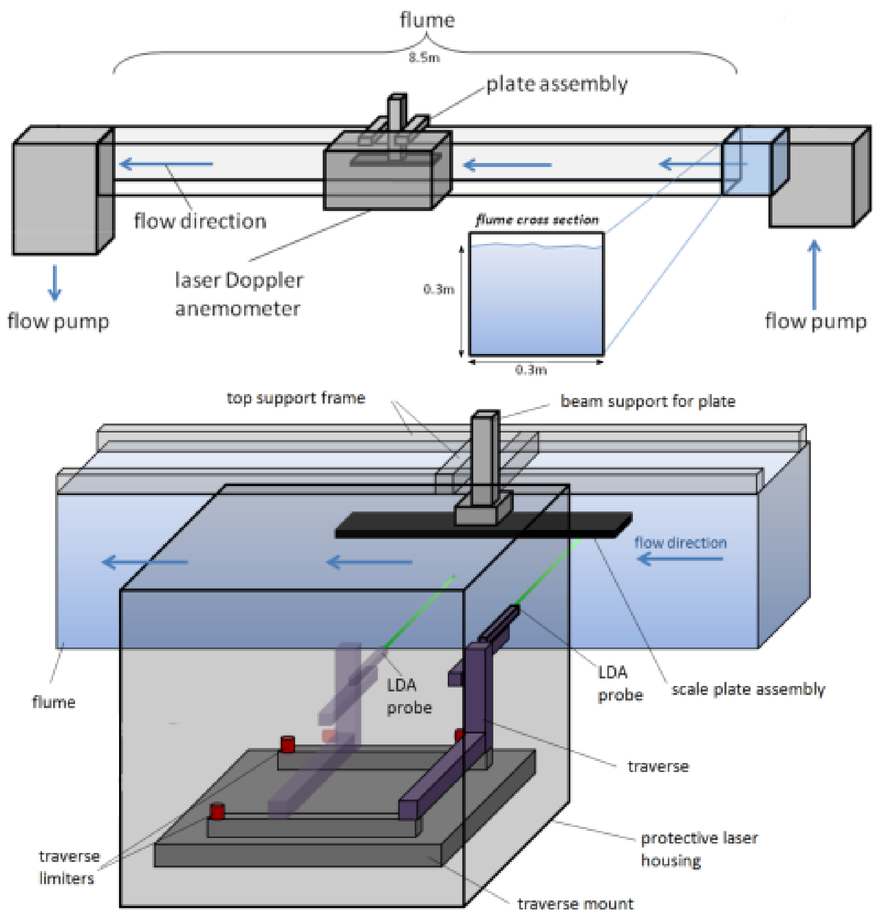

Figure 12: Rig design adapted from Fletcher (2015)

the plate at the most upstream point of the flat section. The streamwise coordinate is defined as x and the wall-normal as y. As discussed in Section 2, the viscous sub-layer exists up to $y^+ \approx 5$. If this is to be measured accurately the wall-normal grid size must be of the same order as the wall-unit length scale, $\delta_\nu = u_\tau/\nu$. In addition to this, the location of the wall must be known to the same order. For this reason the wall-normal zero position is set to lie in the flat plate, such that the first few wall-normal grid points lie in the wall. This ensures that the full velocity profile can be captured. The following grid is defined such that a high spatial resolution is present near the wall which blends into a low resolution in the far field:

$$\Delta = \begin{cases} 0.025, & \text{for } 0 \leqslant y < 2.5, \\ 0.05, & \text{for } 2.5 \leqslant y < 3, \\ 0.1, & \text{for } 3 \leqslant y < 5, \\ 0.5, & \text{for } 5 \leqslant y < 20, \\ 1, & \text{for } 20 \leqslant y < 30, \\ 5, & \text{for } 30 \leqslant y < 75, \end{cases}$$

where the grid spacing, Δ_y, and the wall-normal coordinate, y, are defined in mm. The total number of grid points is 180 which is more than required to capture the profiles accurately. Future experiments will re-evaluate the grid based on the findings of the present study.

The time series measured at each point is passed through a moving average filter in order to remove anomalies. Anomalies are identified if they lie outside the range

$$\mu_{u,2s} - 2\sigma_{u,2s} < u < \mu_{u,2s} + 2\sigma_{u,2s}, \tag{12}$$

where s is half the width of the filter window and u is a component of velocity. $\mu_{u,2s}$ and $\sigma_{u,2s}$ are defined by

$$\mu_{u,2s} = \frac{\sum_{i=-s}^{s} u_i \tau_i}{\sum_{i=-s}^{s} \tau_i}, \tag{13}$$

and,

$$\sigma_{u,2s}^2 = \frac{\sum_{i=-s}^{s} \tau_i (u_i - \mu_{u,2s})^2}{\sum_{i=-s}^{s} \tau_i}. \tag{14}$$

The anomalies identified by the filter were removed from the data set rather than replaced. Other filters were also tested; a global averaging method was found to remove 'real' data due to its inability to differentiate between anomalies and low/high speed structures passing through the probe volume. The filtering method of Goring and Nikora (2002), designed for Acoustic Doppler Anemometry data, was also found to identify more anomalies than expected.

5.3 Preliminary Results

Two sets of results are presented in this section; a time dependence analysis of the means, standard deviations, and the covariance of the two velocity components; and an analysis of the measured profiles. The time dependence study investigates the convergence of statistics as a function of the averaging time. This allows the errors associated with short averaging times to be estimated, and also provides information regarding how much averaging time is required to reduce the error to an acceptable level. The second section investigates the spatial dependency on the flow statistics which will ultimately be used to compare the differences between sharkskin and smooth surfaces.

5.3.1 Time Dependence

Time dependence was assessed at three vertical locations, 400 mm from the upstream end of the plate. These positions were at y =1 mm, 15 mm, and 40 mm. This analysis also investigates how the statistics converge against the number of samples measured. This is dependent on the sampling rate of the LDA, and the local time scale of the flow. It is expected that high local velocities will result in a higher sampling rate.

The probe measured velocities for 300 s at each location for pump speeds of 4 Hz and 8 Hz. The mean streamwise velocity as a function of time is defined as $\mu_u(t)$, whereby μ_u is evaluated between $t = 0$ and t. The standard deviations and covariance are defined using the same notation. Convergence is determined by normalising these quantities against their evaluation over the whole time series. These reference values can be observed in Table 4.

Figures 13 to 17 indicate how the statistics converge as the averaging time, and sample number, increase. For clarity, only the two extreme y positions are plotted. Figure 13 indicates fast convergence for the mean streamwise velocity at y =40 mm for both pump speeds. An averaging window of $\lesssim$ 30 s can reduce the error to below 1 %. As expected, the mean streamwise velocity converges more slowly near the wall. After ~30 s convergence to ~5 % is achieved for the pump frequency of 8 Hz, but only 10 % for

Table 4: Reference values of means, standard deviations, and the covariance of the two velocity components.

Pump Frequency (Hz)	z location (mm)	$\mu_u(300)$ (m/s)	$\mu_v(300)$ (m/s)	$\sigma_u(300)$ (m/s)	$\sigma_v(300)$ (m/s)	$\gamma_{u,v}(300)$ (m^2/s^2)
4	1	0.027081	-0.000173	0.008319	0.000773	-0.000002
4	15	0.091392	-0.000447	0.008947	0.005598	-0.000019
4	40	0.100255	-0.000787	0.008099	0.005211	-0.000011
8	1	0.085152	-0.000843	0.023807	0.003023	-0.000031
8	15	0.185502	-0.001367	0.015663	0.009869	-0.000047
8	40	0.204352	-0.001552	0.013103	0.008496	-0.000027

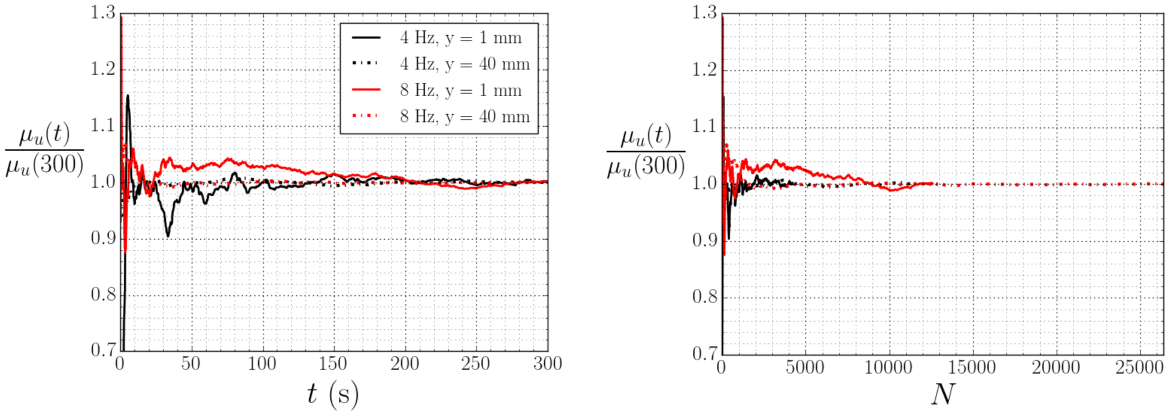

Figure 13: Convergence of the mean streamwise velocity as a function of time (left) and sample number (right).

4 Hz. In order to reduce the low pump frequency error to below 5 % an averaging window of ∼50 s is required. Both pump frequencies require an averaging window of ∼200 s to converge to within a ∼1 % error. In terms of the number of samples, it takes more than twice as many to converge for the higher pump frequency. These results suggest that convergence of the mean streamwise velocity is more dependent on averaging time rather than the number of samples obtained.

Figure 14 indicates very poor convergence for the mean vertical component of velocity, especially for the low pump frequency. This is likely due to the tolerances of the LDA; the recorded wall-normal velocities are of order 0.1 mm/s for the low pump frequency. This is at least two orders of magnitude lower than the streamwise velocity measurements, even close to the wall. For completeness the statistics were not omitted, but the mean wall-normal velocity is rarely published in boundary layer literature.

The standard deviations are important due to their relationship with the turbulent

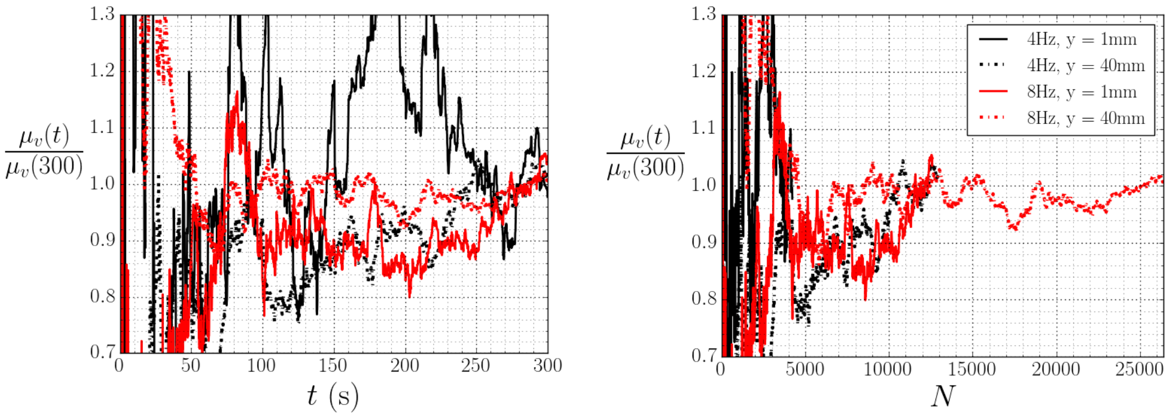

Figure 14: Convergence of the mean wall-normal velocity as a function of time (left) and sample number (right).

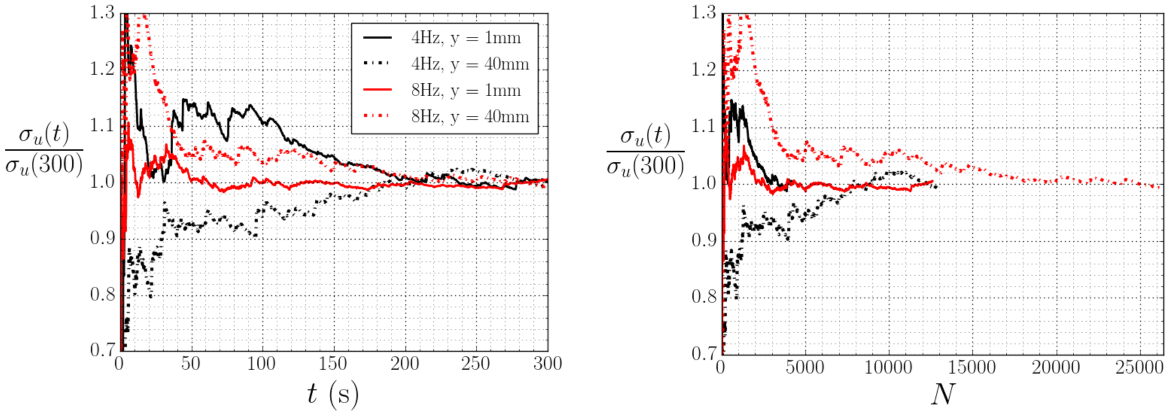

Figure 15: Convergence of the standard deviation of the streamwise velocity as a function of time (left) and sample number (right).

kinetic energy and the Reynolds stresses. As observed in Figure 15, the standard deviations of the streamwise velocity, at a pump frequency of 4 Hz, converge at the same rate for both vertical positions, taking ∼130 s to reduce to a 5 % error, and ∼200 s to reduce to 2 %. In contrast, the standard deviation at y =1 mm converges more quickly than at y =40 mm, for the higher pump frequency. This can be explained by referring to Table 4; for a pump frequency of 4 Hz the magnitude of σ_u is of a similar magnitude for both y locations. This is not the case for the higher pump frequency; at y =1 mm the magnitude of σ_u is larger than at y =40 mm, suggesting that convergence is related to the magnitude of the statistic in question. At y =1 mm the standard deviation reduces to an error of ∼2 % after just 60 s. In contrast, it takes ∼200 s at y =40 mm. Figure 15 also indicates that convergence is more dependent on the averaging time rather than the number of samples. After ∼200 s all four profiles have converged within ∼2 % of their final value, but there is no common sample number that suggests convergence.

The convergence of the wall-normal velocity standard deviations can be observed in Figure 16. After ∼100 s all four profiles converge at the same rate. An error of ∼4 % is obtained after 100 s and ∼2 % after 220 s. Again, convergence appears to be more dependent on the time interval rather than the number of samples.

The covariance of the two velocity components convergences very slowly, as indicated by Figure 17. Even after 300 s, only the near wall point for the high pump frequency indicates reasonable convergence, whereby the error is reduced to ∼2 % after ∼250 s. Although this estimate makes the assumption that $\gamma_{u,v}(300)$ represents the 'true' value. Figure 17 also highlights some sudden jumps in the near wall, low pump speed covariance. This could have arisen from non-physical spikes in the $(u-\mu_u)(v-\mu_v)$ time series. Perhaps the filtering method should be applied to more than just the u and v data sets. However, the other three covariances still predict an error of >10 % after 200 s of averaging time. Clearly, if the Reynolds stresses are to be used to analyse the effect of shark skin then

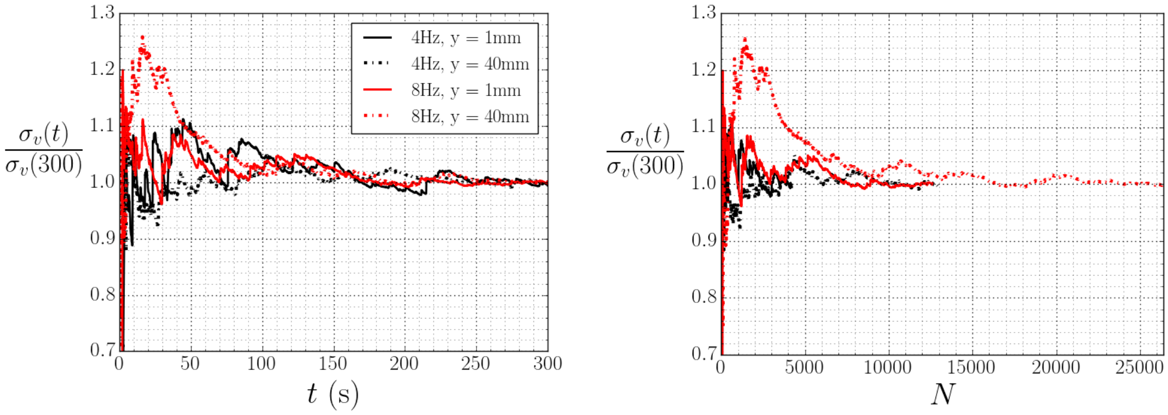

Figure 16: Convergence of the standard deviation of the wall-normal velocity as a function of time (left) and sample number (right).

longer averaging times will be required.

5.3.2 Spatial dependence of the velocity statistics

The means, standard deviations and covariance of velocity are measured along profiles at x =300 mm and x =400 mm. The vertical locations are given in the grid defined in Section 5.2 and profiles are measured for a pump frequency of 4 Hz and 8 Hz. Due to time constraints, velocities were only sampled for 20 s. The errors associated with this are estimated by using the time dependence analysis of Section 5.3.1; the mean streamwise velocity, μ_u, is evaluated over 20 s intervals, throughout the length of the 300 s time series. The mean of the absolute difference between each interval mean and the reference mean, $\mu_u(300)$, is defined as the error. However, since the error can only be estimated at three vertical locations, interpolation is adopted in order to fit the entire profile. Future work will consider many more locations to estimate this error.

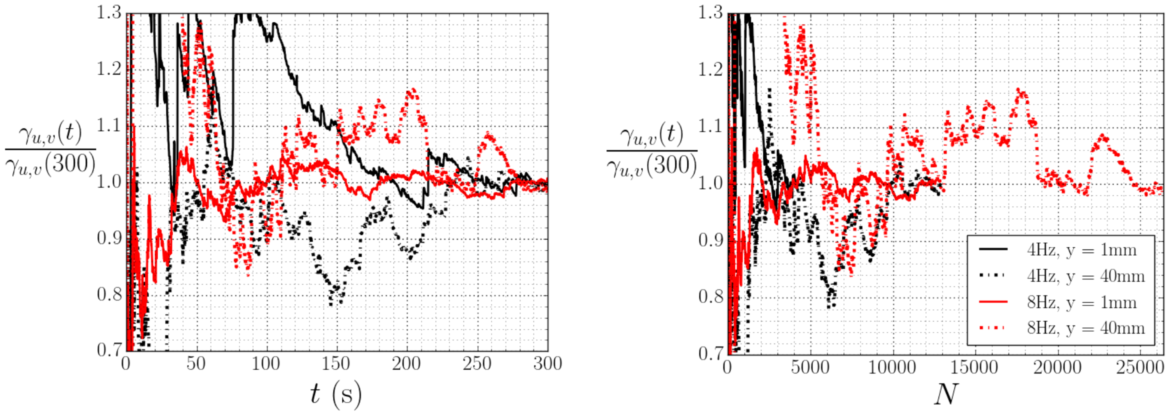

Figure 17: Convergence of the covariance of the streamwise and wall-normal velocities as a function of time (left) and sample number (right).

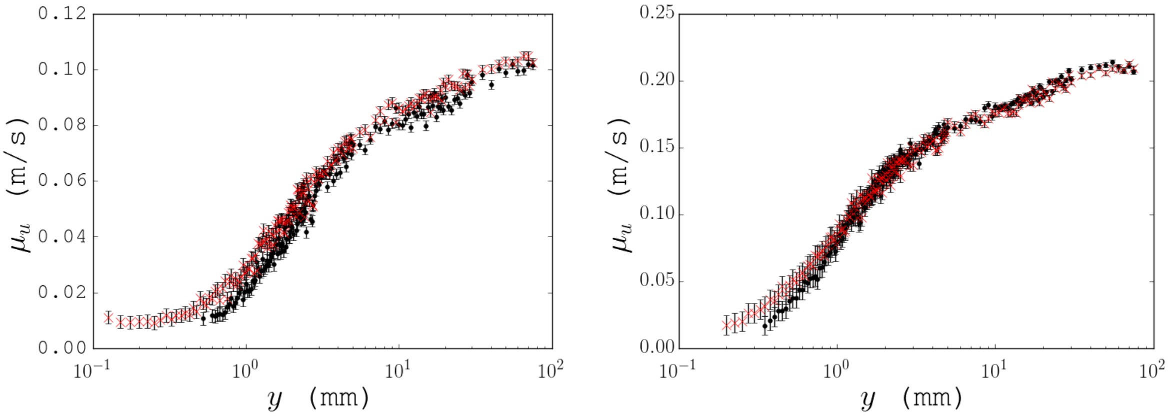

Figure 18: Raw profiles of mean streamwise velocity for pump frequencies of 4 Hz (left), and 8 Hz (right). Symbols represent the following: $\bullet$, μ_u at $x = 300$ mm; $\times$, μ_u at $x = 400$ mm.

The mean streamwise velocity profiles can be observed in Figure 18. The logarithmic region of the 8 Hz pump frequency can be distinguished as the linear trend between $\sim$2 mm and $\sim$20 mm but it is harder to locate for the low pump frequency. This is due to its shorter length and a larger spread in the data, likely due to the short averaging time. However, the viscous and buffer regions are especially well resolved for the mean velocity. Figure 18 also shows a collapse of the $x = 300$ mm and $x = 400$ mm for the higher flow rate, with a small deviation near the wall. This suggests that the velocity profiles are close to fully developed. In contrast, the lower frequency flows indicate a slightly reduced velocity for the entire measured profile. It should be noted that the profiles were only measured up to 75 mm due to experimental constraints. Future experiments will be revised such that half the channel height, $\delta=$ 100 mm, can be measured. The low pump frequency results also indicate more points captured in the downstream profile. This suggests that the plate is not quite flat. However, a difference in 0.4 mm over a distance of 100 mm equates to an angle of $\sim 0.3°$ and can therefore be neglected.

The standard deviation profiles can be observed in Figure 19. The wall-normal fluctuations are captured reasonably well for both pump speeds. The two x locations collapse until $y \approx 1$ mm, at which point the wall-normal standard deviations reach their maximum and a larger spread of the data can be observed. At a pump frequency of 8 Hz the streamwise fluctuations reach a maximum in the buffer region. There is a lot of spread in the data, clearly suggesting that longer averaging times are required. Despite the spread in data, a collapse can be observed in the buffer layer, between the two x profiles. These differentiate nearer the wall, indicating that the fluctuations are of a greater magnitude further along the plate. The 4 Hz standard deviations indicate a much larger error in the streamwise direction. The plot also indicates that there is much more spatial resolution between $y = 1$ mm and $y =$3 mm than is required.

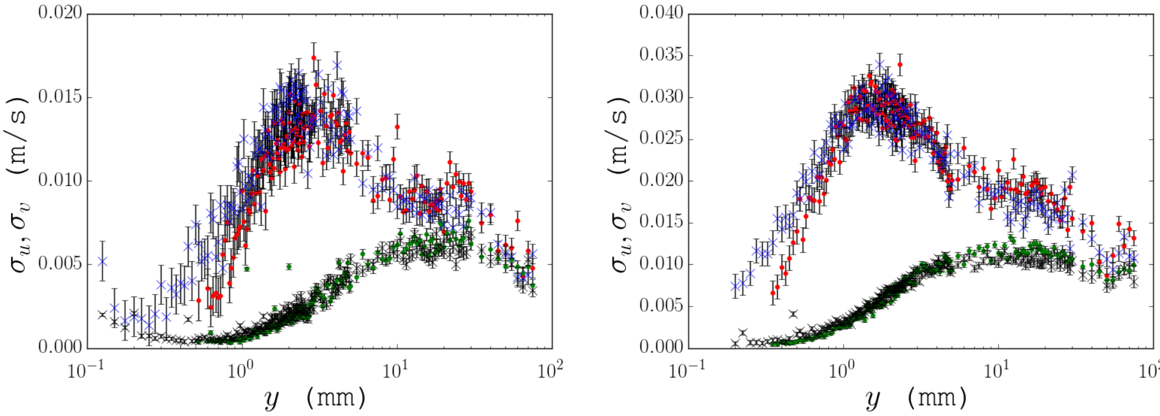

Figure 19: Raw profiles of standard deviations of velocity for pump frequencies of 4 Hz (left), and 8 Hz (right). Symbols represent the following: •, σ_u at $x = 300$ mm; ×, σ_u at $x = 400$ mm; •, σ_v at $x = 300$ mm; ×, σ_v at $x = 400$ mm.

The profiles of velocity covariance can be observed in Figure 20. The covariance indicates a large spread in the data as the distance from the wall increases. The estimated error bars do reflect this increase in uncertainty but the magnitude seems too small in this case. This is likely due to the lack of points used to estimate these errors. It could also be due to the fluctuations in the errors which are not reflected by taking the mean of the absolute error. Future work will investigate the effect of taking into account the standard deviations. It is clear from Figure 20 that if the Reynolds stresses are to be compared between smooth and sharkskin surfaces then a much longer averaging time is required.

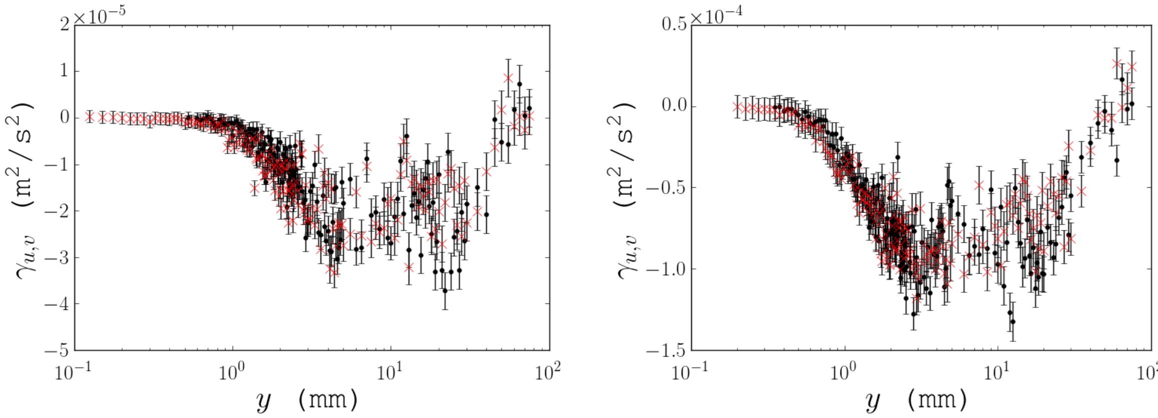

Figure 20: Raw profiles of the covariance of the two velocity components for pump frequencies of 4 Hz (left), and 8 Hz (right). Symbols represent the following: •, $\gamma_{u,v}$ at $x =$300 mm; ×, $\gamma_{u,v}$ at $x =$400 mm.

Estimation of the friction velocity

In order to compare both smooth and sharkskin surfaces the friction velocity must be estimated from the flow field. There are several methods of doing this, such as using the near wall gradients or using the integrated boundary layer equations of a similar form to (4). The present work adopts the Clauser (1956) method, whereby the logarithmic region identified in Figure 3 is fitted with the empirical equations:

$$U^+ = \begin{cases} y^+, & \text{for } y^+ \lesssim 5, \\ \kappa^{-1} \ln y^+ + B, & \text{for } y^+ \gtrsim 30, \end{cases} \tag{15}$$

where U^+ and y^+ are defined by (1). Several challenges are presented with fitting this relationship; the upper bound for the logarithmic layer is dependent on the Reynolds number, and is therefore unknown. In addition to this, the location of the wall has not yet been accounted for in the previous statistics. Subsequently the profile offset needs to be estimated. Since the viscous sub-layer is well resolved, we can estimate the offset by using the equation,

$$y = U\frac{u_\tau^2}{\nu} + \Delta_w, \tag{16}$$

where Δ_w is the offset from the wall and $U = \mu_u$. We adopt least-squares regression to fit the data and subtract Δ_w from the vertical position. The least-squares approach also provides an estimate for u_τ which is subsequently used to estimate the range of vertical positions in the logarithmic region, such that least-squares regression can be applied to

$$U = \frac{u_\tau}{\kappa} \ln y + \frac{u_\tau}{\kappa} \ln \frac{u_\tau}{\nu} + Bu_\tau. \tag{17}$$

Currently the upper bound of the logarithmic region is defined as $y^+ = 150$ in order to ensure the wake region is not captured. As a result, two estimates of the friction velocity are obtained for each profile, one from (16), and one from (17). These can be observed in Table 5. A maximum difference of 20 % can be observed from the two estimates which is a larger magnitude than would be expected between a smooth and sharkskin surface. The dimensionless velocity profile of the 8 Hz pump frequency, based on the logarithmic estimate of u_τ, is presented in Figure 21. The fit agrees well with the logarithmic region

Table 5: Estimates of the friction velocity.

Pump Frequency (Hz)	x location (mm)	u_τ (Viscous estimate) (m/s)	u_τ (log-law estimate) (m/s)	Error (%)
4	300	0.00522	0.00414	20.83
4	400	0.00504	0.00437	13.19
8	300	0.01011	0.00888	12.14
8	400	0.01005	0.00918	08.43

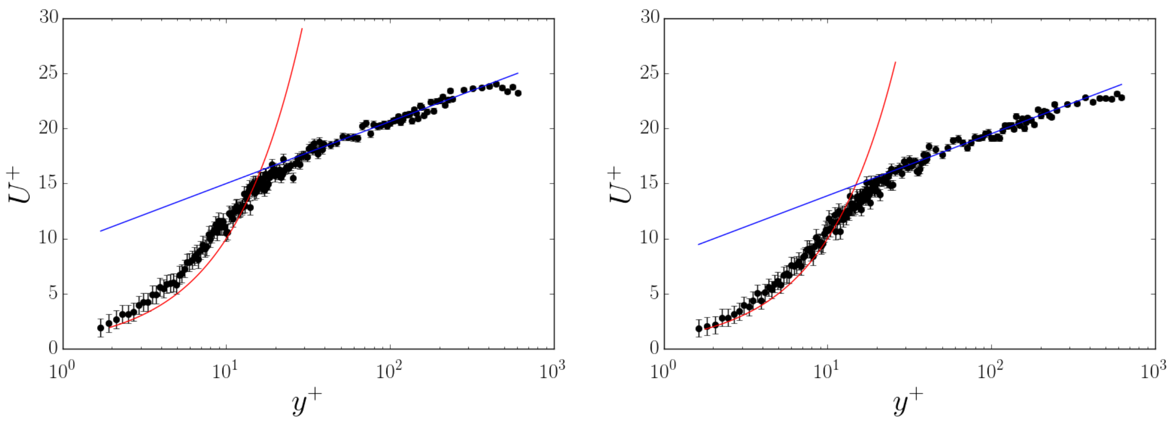

Figure 21: Mean velocity profiles in wall units for a pump frequency of 8 Hz at an x location of 300 mm (left) and 400 mm (right). Red lines represent the estimate of the viscous region, blue lines represent the estimate of the logarithmic region.

but deviates slightly for the viscous region. The $x = 400$ mm profile indicates that the viscous estimate lies within the error bars of the data, although there is still a difference in u_τ predictions of 8.43 %. Further work will investigate the implementation of this method in an attempt to reduce the error. However, other methods of estimating the friction velocity will also be investigated, such as using the near wall gradients of velocity, and an integrated boundary layer method that takes into account the Reynolds stresses. Of course, the accuracy of the later method is dependent on the resolution of the Reynolds stress profile, which will be a priority in future experiments.

5.4 Conclusions and further work

The presented experiments have indicated several adjustments that should be made to the methodology and rig design. The spatial resolution is much higher than required at these low flow rates, especially in the buffer region. In contrast, the averaging time is too short for accurate estimates of the Reynolds stresses, and the standard deviations of velocity. In addition to this, the errors associated with short averaging times have only been estimated at three vertical locations. Future work will carry out experiments on a coarser grid, with longer averaging times, and calculate errors based on more grid points. Furthermore, the methods of estimating u_τ will be re-evaluated before carrying out future experiments.

The current work has only investigated means, standard deviations, and the covariance of the two velocity components. However, there are many other methods to quantify turbulent flows. In particular, investigations into energy spectra will provide information regarding the turbulent structures near the wall. In addition to this, quadrant analysis could be adopted in order to identify sweep and ejection events for both smooth and sharkskin surfaces.

6 CAD: Replication of a shark scale

This Section details the process adopted to replicate and simplify a *Poracanthodes sp.* fish scale (sampled by Fletcher (2015)) for fluid dynamic analysis. This particular scale was chosen due to its relatively simple geometry. Other sampled scales included other geometric features, such as riblets, which are not yet of interest. The implications of these additional features will be investigated through the parameter study. The Computer Aided Design (CAD) process, carried out using CREO Parametric software, is required in order to create an array of scales suitable for manufacture and LDA experimentation. The CAD model is also required in order to carry out numerical analysis; a body fitted mesh will be constructed using the CAD in order to adopt finite volume methods.

The scale sample, provided by Fletcher (2015), is displayed in figure 22. It can be observed from this image that there are many sharp edges that have been introduced, possibly by a lack of resolution from the scanning equipment, defects on the scale sample, or damage to the sample. There are also many asymmetries that exist, such as the wave-like shapes on the trailing edge of the scales. These features are likely due to the discrepancies between scale samples; even scales in tightly packed arrays are known to vary in geometry from scale to scale (Fletcher, 2015). In addition to this, a large portion of the scale is embedded in the dermis of the fish and therefore has no effect on the hydrodynamics of the scale. For these reasons a simplified scale is created, based on the *Poracanthodes sp.* sample. The simplified replica removes the sharp faceted features, the asymmetries and the portion of the scale that lies underneath the fish dermis.

6.0.1 Methodology

A coordinate system is fitted to the scale and 10 datum planes are created in the xz plane with equal spacings between the first 7 and last 3 planes. The first set of planes extend

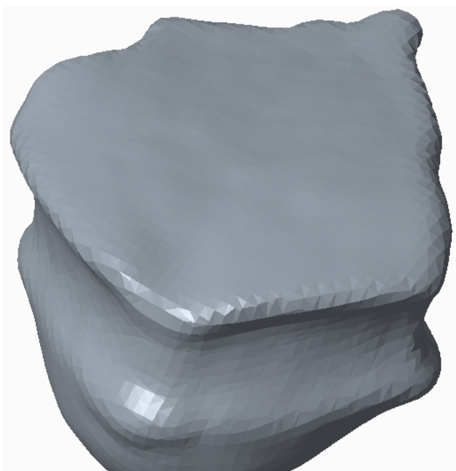

Figure 22: *Poracanthodes sp.* sample from Fletcher (2015).

to the point of maximum width of the sample and the last three are placed in order to capture the steep gradients beyond this point. A sketch is created at each of these planes resembling the cross section of the scale sample but using primitive shapes that can later be parametrised. An example of this is presented in Figure 23;

the wave-like shapes on the downstream section of the scale has been removed and the sketch is symmetric about the central axis. This is achieved by using three arcs connected by tangential lines, reducing each section to three radius parameters, three vertical positions and a single horizontal position (as observed in Figure 23). Each sketch can therefore be represented by a displacement from the $y = 0$ plane and 7 dimensions defining the sketch section. This makes parameter studies straight forward to implement in future work.

The sketches are blended together using a 'protrusion blend' function, creating the CAD model on the right of Figure 24. An undesirable feature of this technique is that the top surface is orthogonal to the defined datum plane. In order to create a more natural curved surface a warping tool, unique to Creo Parametric, is adopted. This tool creates a mesh around the object and allows free-hand manipulation of the surface by moving the mesh nodes. This process allows an organic Scale to be created which more closely resembles that of the original sample. However, parametrising the 'warping' tool is non-trivial. Further work in this area will be carried out in order to develop a more

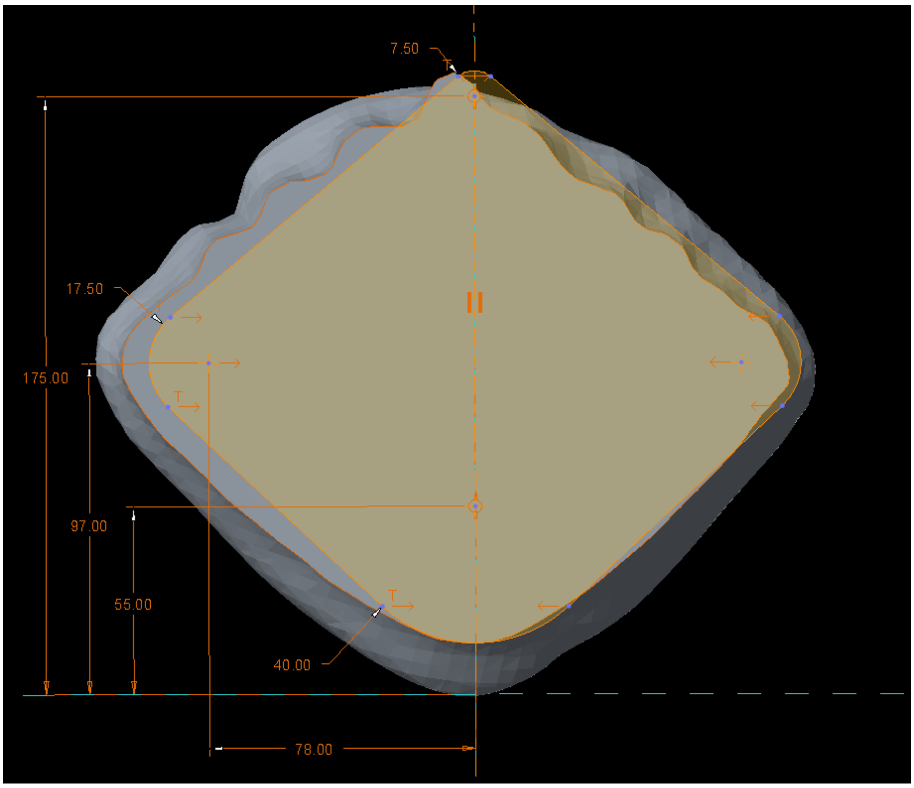

Figure 23: A comparison between a simplified cross section and the sampled scale cross section. The dimensions are scaled after the simplified scale is generated.

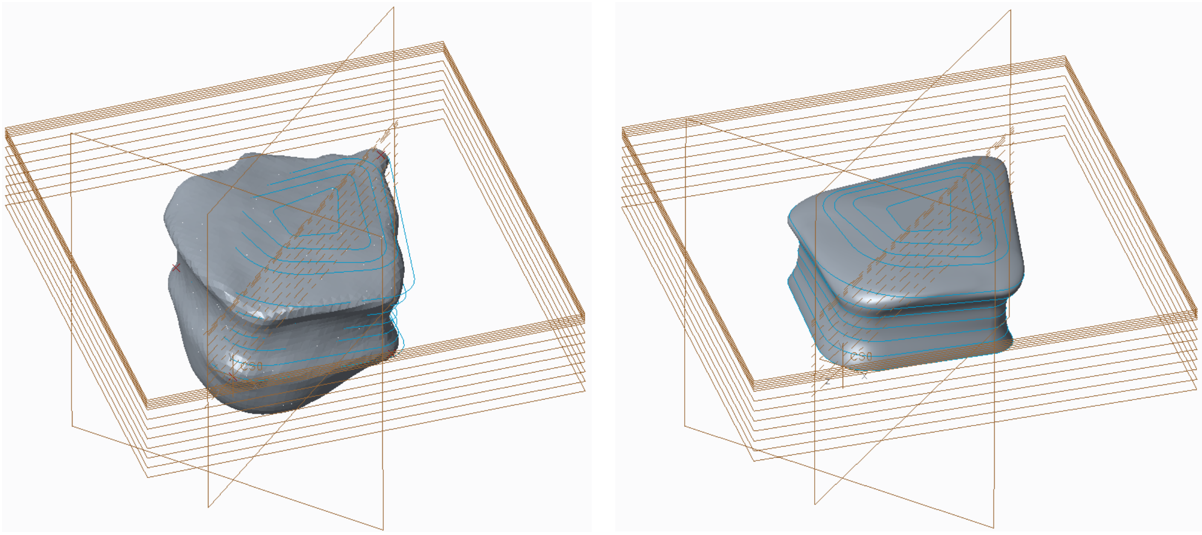

Figure 24: Comparison of sampled scale (left) and simplified scale (right) with overlaying primitive cross sections displayed.

systematic approach, but for initial experimentation this 'one-off' scale is appropriate.

The final scale replica is compared against the scanned sample in Figure 26. The model is scaled to a height of $H^{+} \sim 10$ at a Reynolds number of $Re_{\tau} = 180$ for preliminary meshing experiments. This will later be scaled to a suitable size for both 3D printing, LDA experiments and a high resolution LES. The scales are arranged into a staggered array (Figure 27) with an addition two parameters to define; a spacing in x and in z. The exploitation of this periodic arrangement, through the use of CFD, will be discussed in Section ??.

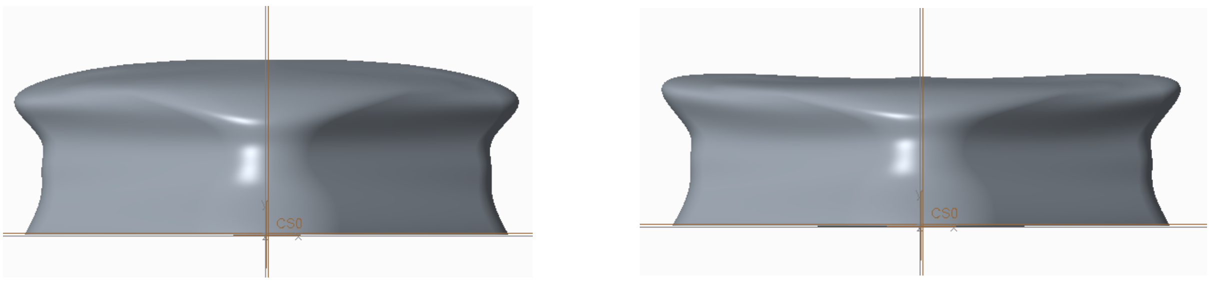

Figure 25: Comparison of blended scale (left) and warped scale (right).

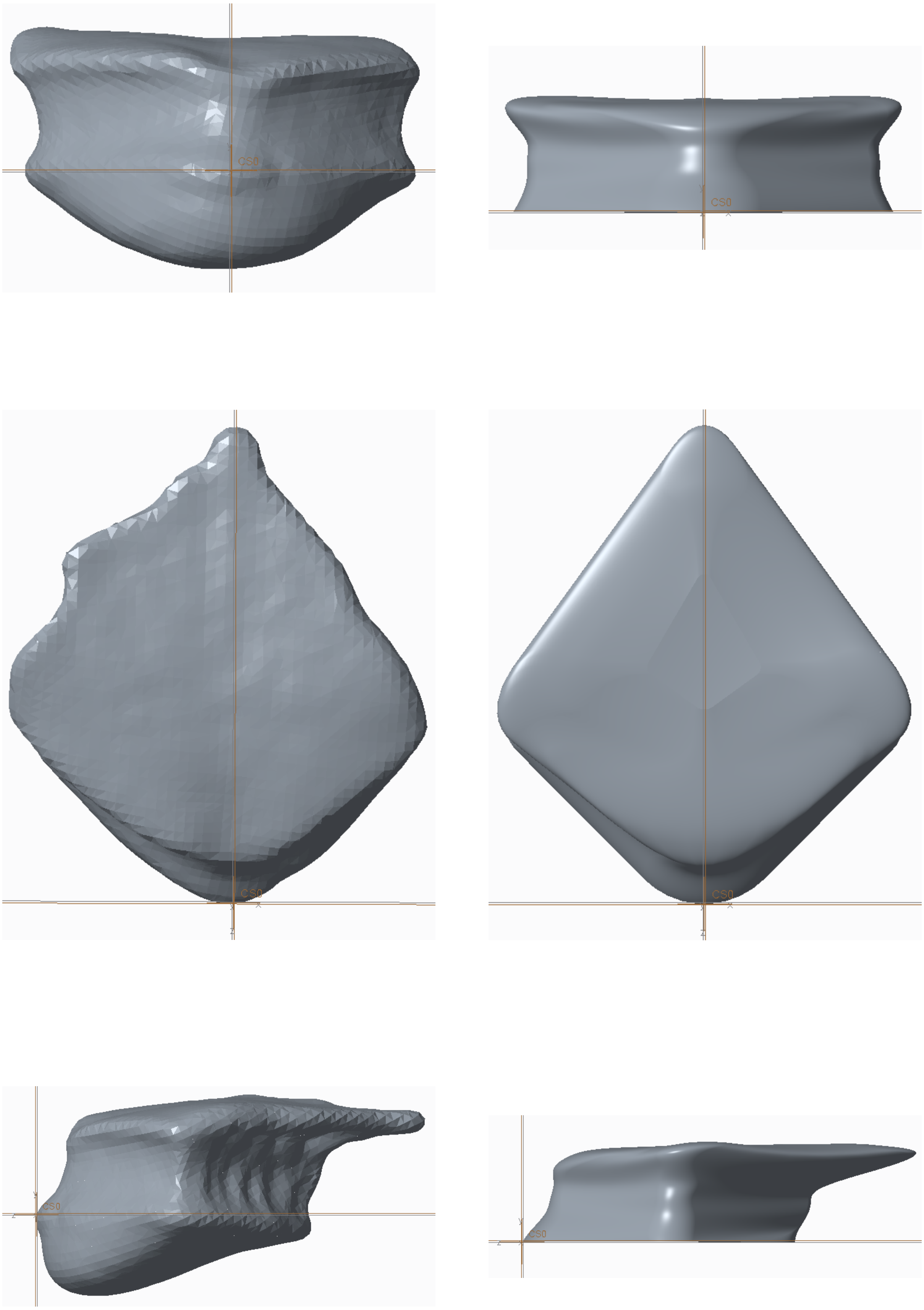

Figure 26: Comparison of sampled scale (left) and simplified scale (right).

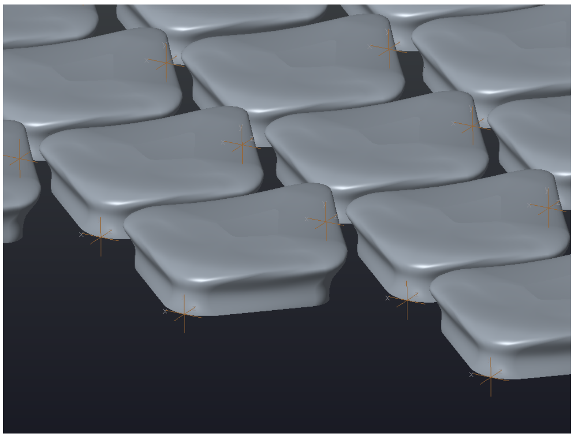

Figure 27: Array of staggered scales for 3D printing.

6.1 Application of Reynolds-Averaged Navier-Stokes to a periodic shark scale domain

This section details the mesh independence study of the flow over a periodic array of scales using a RANS turbulence closure. Section 2 indicated a large gap in the literature concerning the effect of shark scale geometry on a flow. RANS methods have the potential to investigate this without large expense, but requires validation. When available, the results of the present study will be validated against LES data.

6.1.1 Mathematical model

The present work adopts a steady state RANS turbulence closure using OpenFOAM; an open source finite volume code. The fundamental equations are the Reynolds averaged equations, first introduced in Section 2, and the continuity equation. These are defined as,

$$\langle U_j \rangle \frac{\partial \langle U_i \rangle}{\partial x_j} = -\frac{\partial \langle P \rangle}{\partial x_j} + \nu \left(\frac{\partial \langle U_j \rangle}{\partial x_i} + \frac{\partial \langle U_i \rangle}{\partial x_j} \right) + \frac{\partial \langle u_i u_j \rangle}{\partial x_j}, \tag{18}$$

and the continuity equation,

$$\frac{\partial \langle U_i \rangle}{\partial x_i} = 0, \tag{19}$$

where $\langle\rangle$ represents the ensemble average. This particular work adopts the $k-\omega$ Shear Stress Transport (SST) model, first proposed by Menter (1994). This closure estimates the Reynolds stresses by solving a transport equation for the turbulent kinetic energy, k, and the turbulent frequency, ω. The standard $k-\omega$ model is known for its ability to resolve boundary layer flows more accurately than other two-equation alternatives, such as $k-\epsilon$. However, it has failed to replace the $k-\epsilon$ model as the industry standard due to its poor performance in freestream flows (Menter et al., 2003). This issue is accounted for in the $k-\omega$ SST model by adding an additional term to the ω equation. The result is essentially a blending between the near wall $k-\omega$ model and the freestream $k-\epsilon$ model.

There are many other turbulence closures that could be appropriate for this problem. The two equation $k - \omega$ SST model was chosen as a compromise between the more accurate, but computationally expensive, Reynolds Stress Transport equations, and the less accurate, but cheaper, one-equation models. The solution dependency on turbulence closure will be investigated after obtaining a mesh independent solution.

The $k-\omega$ SST model adopts the turbulent viscosity hypothesis, whereby the Reynolds stresses are estimated by,

$$\langle u_i u_j \rangle = \frac{2}{3} k \delta_{ij} - \nu_T \left(\frac{\partial \langle U_i \rangle}{\partial x_j} + \frac{\partial \langle U_j \rangle}{\partial x_i} \right), \tag{20}$$

where ν_T is the turbulent viscosity. The $k-\omega$ SST model solves two additional transport equations for the turbulent kinetic energy, k, and the turbulent frequency, ω. These parameters are related by the rate of turbulent dissipation, $\epsilon = \omega k$. The turbulent viscosity is assumed to be related to k and ω by,

$$\nu_T = \frac{a_1 k}{\max\left(a_1 \omega, F_1 \sqrt{2 S_{ij} S_{ij}}\right)}, \tag{21}$$

where a_1 is an empirical constant, F_1 is a blending function, and S_{ij} is the rate of strain tensor,

$$S_{ij} = \frac{1}{2} \left(\frac{\partial \langle U_i \rangle}{\partial x_j} + \frac{\partial \langle U_j \rangle}{\partial x_i} \right). \tag{22}$$

The blending function is a hyperbolic tangent function, such that it takes the value 0 near the wall and 1 far from the wall. The transport equation for k is defined as,

$$\frac{\partial (\langle U_j \rangle k)}{\partial x_j} = \mathcal{P} - \beta^* \omega k + \frac{\partial}{\partial x_j} \left[(\nu + \sigma_k \nu_T) \frac{\partial k}{\partial x_j} \right], \tag{23}$$

where β^* and σ_K are empirical constants, and $\mathcal{P}$ is the production of turbulent kinetic energy,

$$\mathcal{P} = -\langle u_i u_j \rangle \frac{\partial \langle U_i \rangle}{\partial x_j}. \tag{24}$$

(24) is solved by using the definition of $\langle u_i u_j \rangle$ in (21). The equation for ω is given by,

$$\frac{\partial (\langle U_j \rangle \omega)}{\partial x_j} = \frac{\alpha}{\mu_T} \mathcal{P} - \beta \omega^2 + \frac{\partial}{\partial x_j} \left[(\nu + \sigma_w \nu_T) \frac{\partial \omega}{\partial x_j} \right] + 2(1 - F_2) \frac{\sigma_d}{\omega} \frac{\partial k}{\partial x_j} \frac{\partial \omega}{\partial x_j}, \tag{25}$$

where α, β, σ_ω, and σ_d, are empirical constants, $\mu_T = \rho \nu_T$, and F_2 is a blending function of the same form as F_1. The choices of F_1, F_2, and the empirical constants, are detailed by Menter (1994). The three component momentum equation, (18), continuity equation, (19), transport of kinetic energy equation, (23), and the transport of turbulent frequency equation, (25), are our closed system of equations.

6.1.2 Numerical implementation

The system of equations, defined in Section 6.1.1, are discretised using finite volume methods. Gradient and Laplacian terms are discretised using standard Gaussian integration. Linear interpolation is adopted in order to calculate face fluxes from the variables stored at cell centres. In order to ensure stability, the interpolation scheme of the convective terms is a mixture of upwind and linear methods, whereby in regions of rapidly changing gradient an upwind scheme is adopted (but still accurate to second order). The SIMPLE algorithm of Caretto et al. (1973) is adopted in order to couple the continuity and momentum equations. The semi-discrete form of (18) can be written as

$$\boldsymbol{C}\boldsymbol{u}^{*} = \boldsymbol{A}\boldsymbol{u}^{*} + \boldsymbol{H'}\boldsymbol{u}^{*} = \boldsymbol{r} - \nabla \boldsymbol{P}^{n}, \tag{26}$$

The PISO algorithm (Pressure-Implicit with Splitting of Operators) of Issa (1986) is adopted, whereby a pressure equation is derived from the momentum (34) and continuity equations (35). The PISO scheme operates using a two-step process: A predictor step and a corrector step. The semi-discrete form of (34) can be written as

$$\boldsymbol{C}\boldsymbol{u}^{*} = \boldsymbol{A}\boldsymbol{u}^{*} + \boldsymbol{H'}\boldsymbol{u}^{*} = \boldsymbol{r} - \nabla \boldsymbol{P}^{n}, \tag{27}$$

where $\boldsymbol{C}$ represents the implicit coefficient array, $\boldsymbol{u}^{*}$ is the predicted velocity, $\boldsymbol{r}$ is the explicit source terms and $\boldsymbol{P}^{n}$ represents the kinematic pressure at the previous time step. The matrix $\boldsymbol{C}$ can be split into diagonal and off diagonal components, $\boldsymbol{C} = \boldsymbol{A} + \boldsymbol{H'}$, and the linear equation (49) can be solved for $\boldsymbol{u}^{*}$. A Gauss-Seidel solver is adopted to solve this system, completing the predictor step. (49) can be manipulated in order to derive an equation to correct both the velocity and pressure from the predicted velocity:

$$\boldsymbol{A}\boldsymbol{u}^{**} + \boldsymbol{H'}\boldsymbol{u}^{*} = \boldsymbol{r} - \nabla \boldsymbol{P}^{*}, \tag{28}$$

$$\boldsymbol{u}^{**} = \boldsymbol{A}^{-1}\boldsymbol{H} - \boldsymbol{A}^{-1}\nabla \boldsymbol{P}^{*}, \tag{29}$$

where $\boldsymbol{H} = \boldsymbol{r} - \boldsymbol{H'}\boldsymbol{u}^{*}$. The inversion of $\boldsymbol{A}$ is trivial since it is symmetrical. By recognising that $\nabla \boldsymbol{u}^{**} = 0$, a Poisson equation for the corrected pressure can be derived:

$$\nabla^{2}(\boldsymbol{A}^{-1}\boldsymbol{P}^{*}) = \nabla \cdot (\boldsymbol{A}^{-1}\boldsymbol{H}). \tag{30}$$

This Laplacian equation is solved using a Geometric-algebraic multi-grid solver in order to update the pressure. The corrected velocity equation (51) is then solved to update the velocity. In order to ensure second order accuracy, (52) and (51) and solved twice, as recommended by Issa (1986). Equations (47) and (48) are discretised using the same method as the momentum equation and solved using a Gauss-Seidel solver. All equations are iteratively solved until a tolerance of 10^{-8} is met. An adaptive time-stepping scheme is adopted in order to ensure the Courant number does not exceed 0.5. Statistical averaging is carried out between the time intervals $t = 10\delta/u_\tau$ and $t = 40\delta/u_\tau$. This interval is much smaller than those adopted by Kim et al. (1987) and Vreman and Kuerten (2014), the impact of which will be discussed in Section 6.2.3.

Post-processing is carried out in MATLAB; Statistical quantities, such as means and standard deviations, are looped through each time-step directory and averaged in x and z. The results of which are compared to those of a spectral DNS code of Vreman and Kuerten (2014).

- SIMPLE .. - solution method - linear algebra ... - -iterative method to mesh it ...? -convergence !!! how do we check?

over the domain observed in Figure 28, using finite volume methods. The CAD model, defined in Section 6, is arranged in a staggered array, the dimensions of which can be observed in Figure 29, where H_s is the height of the scale. The three points, x_1, x_2, and x_3, are used to define wall-normal lines in which data is plotted to assess mesh independence (Discussed in Section ......). Since the fields solved by the RANS formulation are ensemble averaged, we can assume that the flow over each scale is identical. We therefore define periodic boundary conditions in the streamwise (x) direction, and symmetry boundaries in the z direction. The shark scale scale surface is placed at the base of the channel, $y = 0$, and a flat wall is placed at $y = 2\delta$, where δ is the half-channel height. The bulk flow Reynolds number is set to $Re_b = \delta U_b/\nu = 13500$, where U_b is the bulk velocity. For a smooth walled channel, this corresponds to a shear Reynolds number of $Re_\tau = 395$. This particular Reynolds number is commonly adopted in channel flow literature which allows validation to occur. The wall-unit length scale is therefore $\delta_\nu = u_\tau \nu/u_\tau = 1/395$ which is used to estimate the cell sizes when constructing the meshes observed in Figure 28.

SnappyHexMesh software is used to mesh the domain. The refinement is based on a

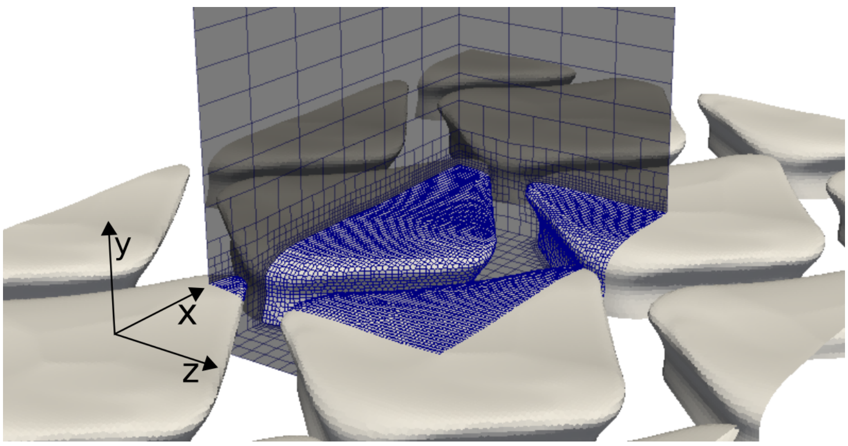

Figure 28: Domain ...

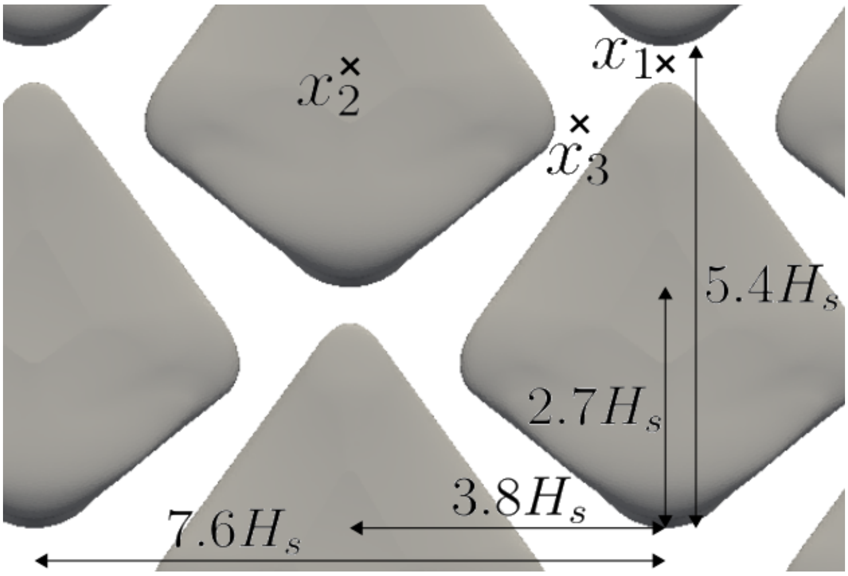

Figure 29: Domain ...

cell level specification, whereby each level splits the cell size of the previous level into 8 smaller cells. Level 0 corresponds to the base mesh size, and a level 1 cell would have each of its edges halved in length. The effect of this can be observed in Figure 30. As the distance from the scales increases, there are several jumps in cell size before reaching that of the base mesh. The location of these jumps, the size of the base mesh, and the maximum level size, are varied between each mesh case.

Three cases are presented in this work, each with a mesh of increasing resolution. By using estimated wall-unit length scale of $\delta_\nu = 1/395$, the mesh is created in wall units. The scale height is set to $H_s^+ = 20$, which will be varied in future experiments. Using the periodic dimensions specified in Figure 29, this corresponds to a domain size of $5.4H_s \times 2\delta \times 7.6H_s = 108 \times 790 \times 152$ in wall units. The three meshes can be observed in Figure 30, and the statistics of each case are presented in Table 6. At least 90 % of the cells in the domain lie below $y^+ < 40$ for each of the cases. case C1 is the 'coarse' solution, with a maximum cell size of 18, and large jumps between cell sizes. C2 has finer cells but still has large jumps. C3 is the same specifications as C2 but has smoother

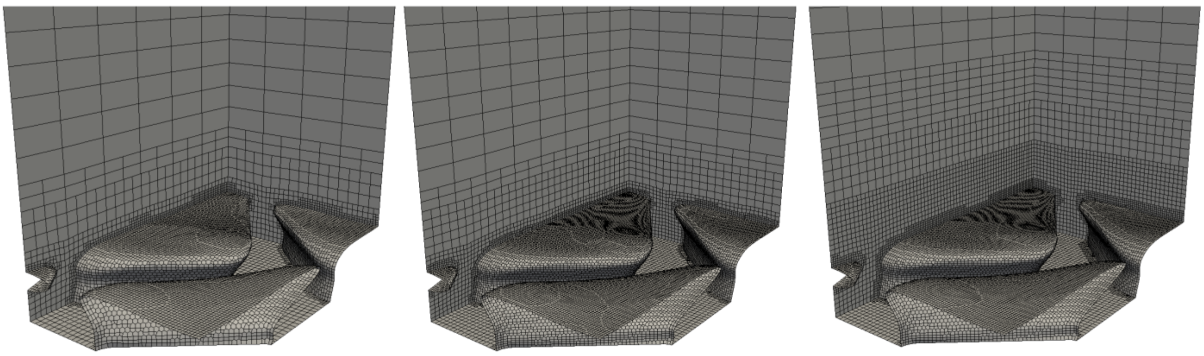

Figure 30: meshes ...

Table 6: ....

Case	Max. cell size Δy^+_{max}	Total cell count N_t	Cell count near scales $N(y^+ < 40)$	Number of faces on the scales N_s
C1	18	39396	37572	7296
C2	14	75417	71617	12571
C3	14	117065	113105	12167

transitions i.e more cells in each layer. The size of the cells covering the STL shark scale is very similar for C2 and C3 cases.

- scale height -mesh parameters of three test cases are in table -and in fig. -should be noted that in order to resolve these relatively large scales we need ¿90% of the cells to be below yPlus = 40 i.e mostly below buffer layer. -cell level over scales is defined

-

Dependency analysis of RANS methods on a periodic shark scale domain. Dependencies include MI, DI, model I, Numerics I, Tol I ... The results will form the basis for the mesh resolution for the LES and the RANS studies. Before carrying out further RANS the results will be validated against a LES.

6.1.3 Problem definition

As discussed? The Reynolds equations are given by

-present k and epsilon equations -indicate what each term is - including the weighting factor -Then introduce the FV method and how equations are discretised over our domain - BC.

6.1.4 Results and discussion

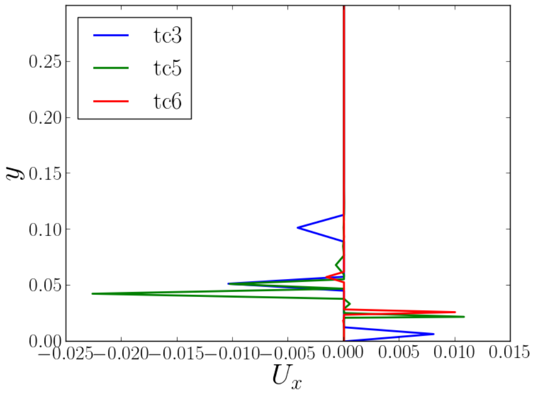

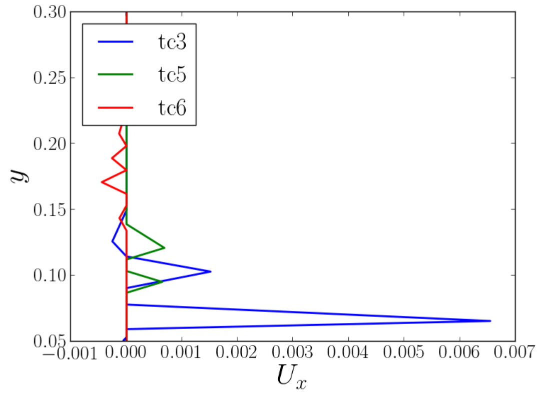

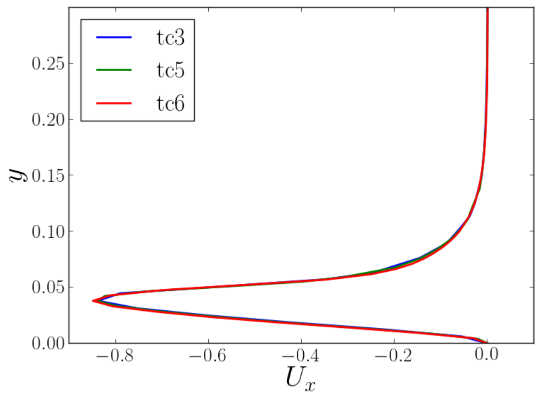

Contour plots: For a scalar, ϕ, we assess independence by interpolating the solution over the scale surface onto the finest STL scale surface. This ensures that cells coincide and solutions can be directly compared. The reference scalar ϕ_{REF} is the solution of the finest mesh. It is scaled such that its minimum value is 0 and maximum is 1:

$$\overline{\phi}_{\mathrm{REF}} = \frac{\phi_{\mathrm{REF}} - \min(\phi_{\mathrm{REF}})}{\max(\phi_{\mathrm{REF}}) - \min(\phi_{\mathrm{REF}})}. \tag{31}$$

Similarly, ϕ, the coarse mesh solution, is translated to a minimum value of 0 and then scaled by the same amount as ϕ_{REF}:

$$\overline{\phi} = \frac{\phi - \min(\phi)}{\max(\phi_{\mathrm{REF}}) - \min(\phi_{\mathrm{REF}})}. \tag{32}$$

The error is defined as the root-mean-square of the difference between ϕ and ϕ_{REF}:

$$\mathrm{error}(\phi)\sqrt{(\overline{\phi}_{\mathrm{REF}} - \overline{\phi})^2} \tag{33}$$

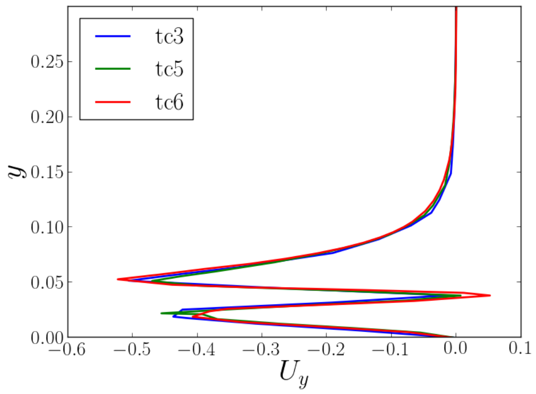
tc3
tc5
tc6
y
U_y

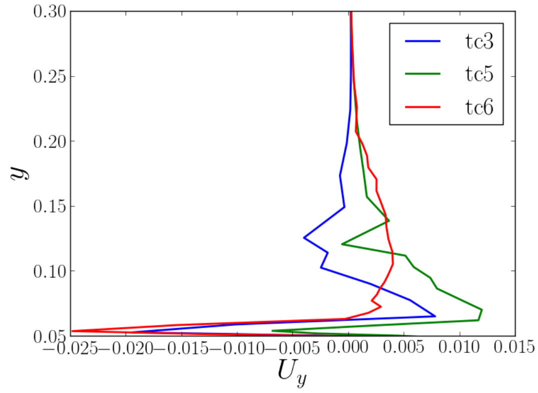
tc3
tc5
tc6
y
U_y

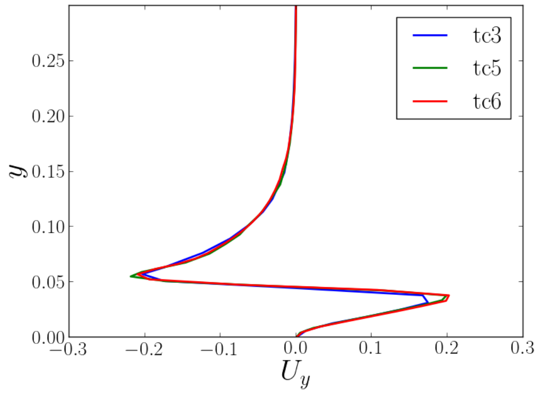
tc3
tc5
tc6
y
U_y

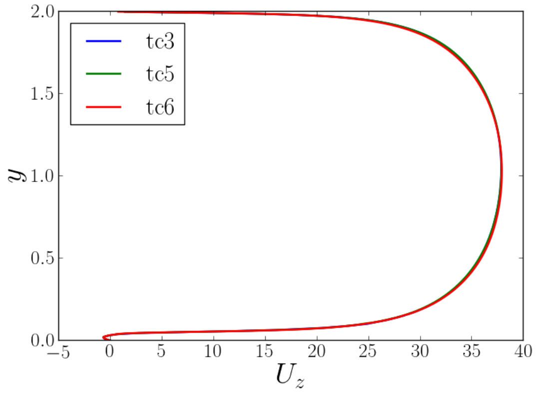
tc3
tc5
tc6
y
U_z

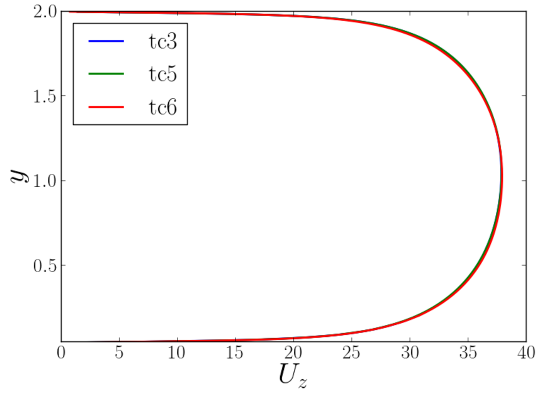
tc3
tc5
tc6
y
U_z

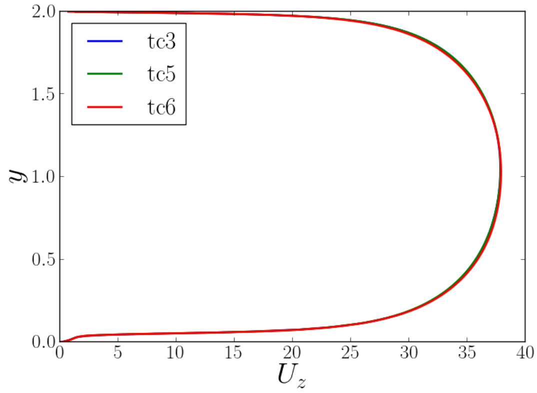
tc3
tc5
tc6
y
U_z

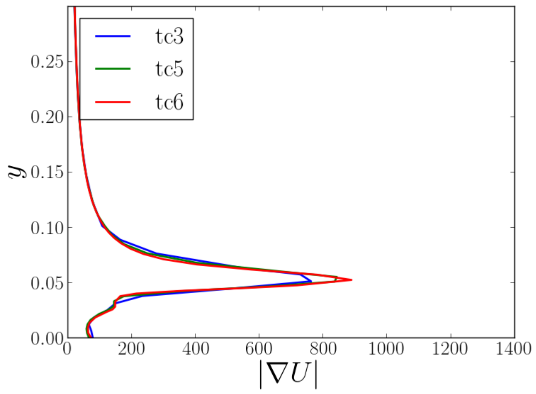
tc3
tc5
tc6
y
0.00
0.05
0.10
0.15
0.20
0.25
0
200
400
600
800
1000
1200
1400
$|\nabla U|$

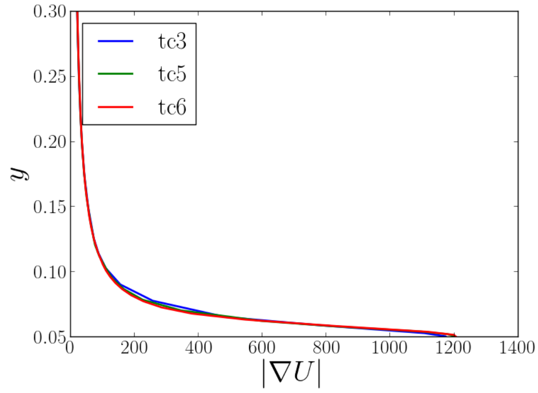
tc3
tc5
tc6
y
0.05
0.10
0.15
0.20
0.25
0.30
0
200
400
600
800
1000
1200
1400
$|\nabla U|$

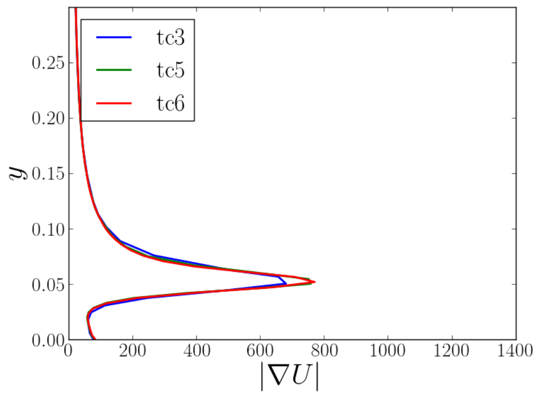
tc3
tc5
tc6
y
0.00
0.05
0.10
0.15
0.20
0.25
0
200
400
600
800
1000
1200
1400
$|\nabla U|$

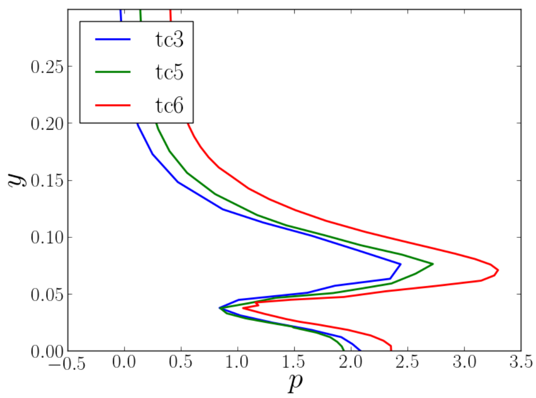
tc3
tc5
tc6
y
0.00
0.05
0.10
0.15
0.20
0.25
−0.5
0.0
0.5
1.0
1.5
2.0
2.5
3.0
3.5
p

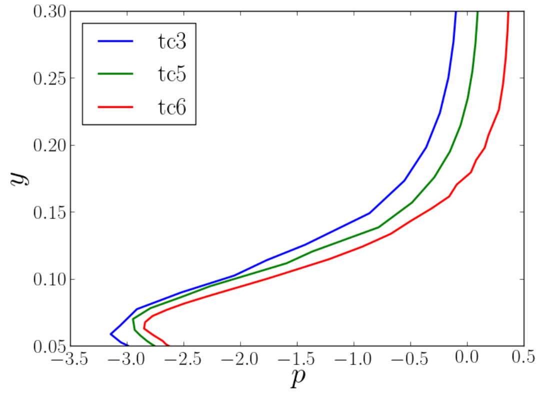
tc3
tc5
tc6
y
0.05
0.10
0.15
0.20
0.25
0.30
−3.5
−3.0
−2.5
−2.0
−1.5
−1.0
−0.5
0.0
0.5
p

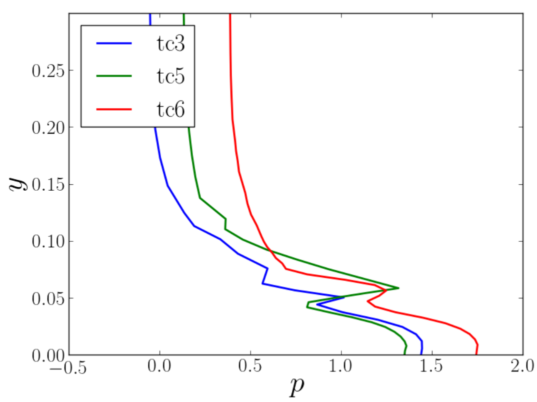
tc3
tc5
tc6
y
0.00
0.05
0.10
0.15
0.20
0.25
−0.5
0.0
0.5
1.0
1.5
2.0
p

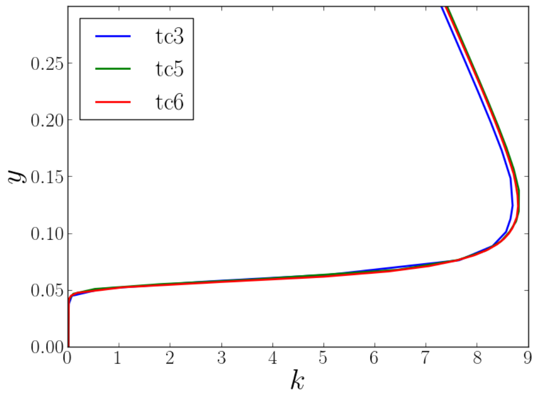
tc3
tc5
tc6
y
0.00
0.05
0.10
0.15
0.20
0.25
0 1 2 3 4 5 6 7 8 9
k

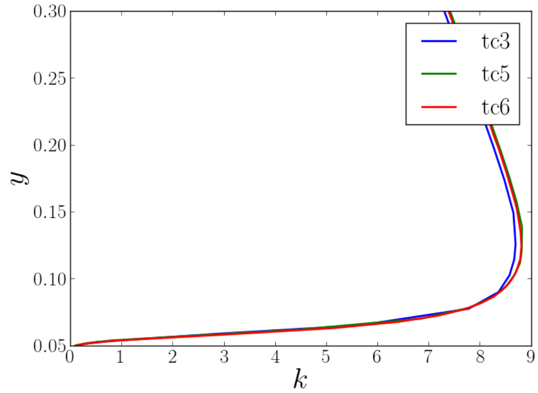
tc3
tc5
tc6
y
0.05
0.10
0.15
0.20
0.25
0.30
0 1 2 3 4 5 6 7 8 9
k

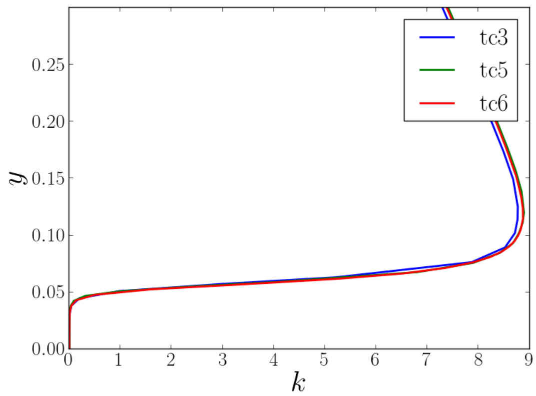
tc3
tc5
tc6
y
0.00
0.05
0.10
0.15
0.20
0.25
0 1 2 3 4 5 6 7 8 9
k

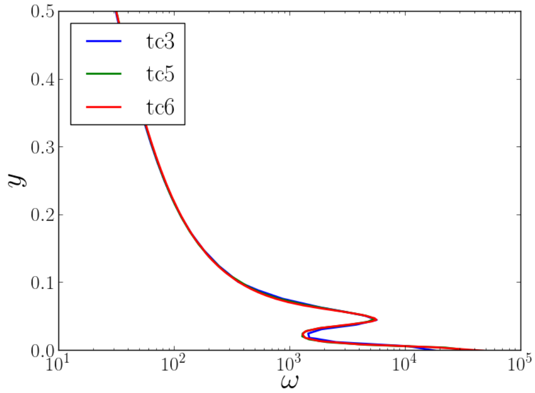
tc3
tc5
tc6
y
0.0
0.1
0.2
0.3
0.4
0.5
10^1 10^2 10^3 10^4 10^5
ω

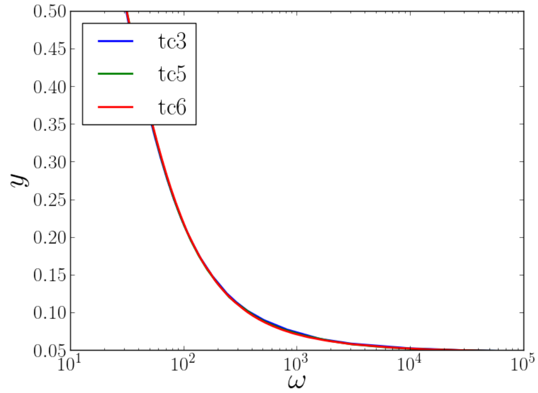
tc3
tc5
tc6
y
0.05
0.10
0.15
0.20
0.25
0.30
0.35
0.40
0.45
0.50
10^1 10^2 10^3 10^4 10^5
ω

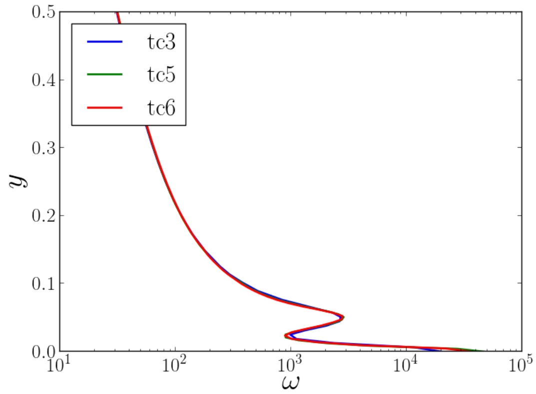
tc3
tc5
tc6
y
0.0
0.1
0.2
0.3
0.4
0.5
10^1 10^2 10^3 10^4 10^5
ω

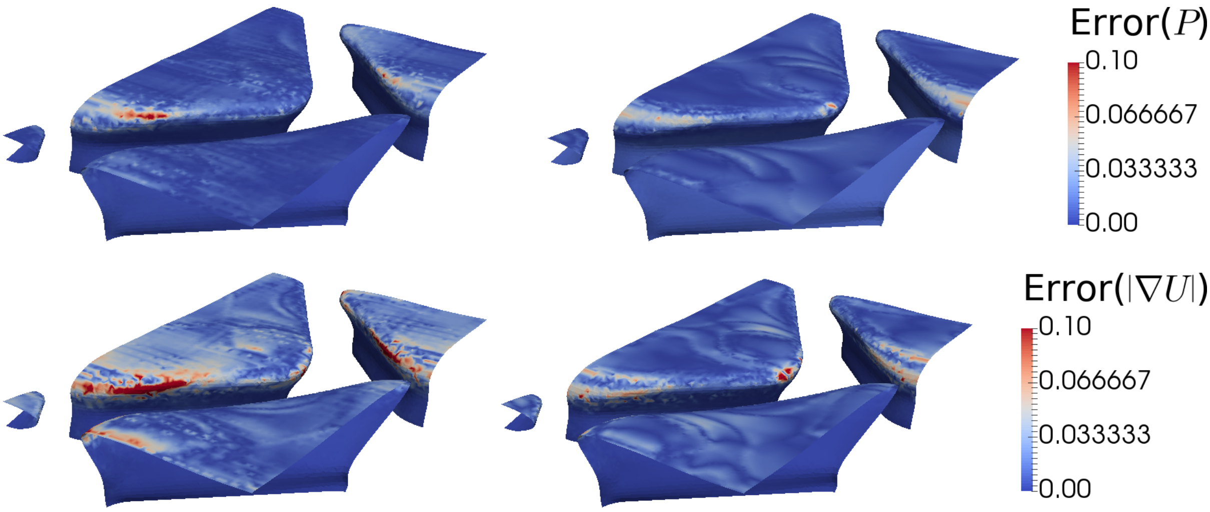

Introduction: - what are we doing, why, how .. dependency studies -MI, DI, models, tolerances, disc. schemes etc. -Eventually validate against LES -Then we can start varying parameters to see effects on the flow field Methodology: - meshing parameters and models used - show domain and BCs, -numerical methods, Results: - MI results for contour plots over surface, profile plots in wall-normal direction.

6.2 Large eddy simulation of a channel flow

In order to exploit periodicity, an infinitely long and wide channel flow with scales on one wall will be simulated. Large-eddy simulation will be adopted in order to model the flow at a feasibly high resolution for a bulk Reynolds number greater than $Re_b = 20\,000$. The precise Reynolds number will be determined later this year when designing the LDA experiments. Before implementing the LES on a channel flow with scales, the code is validated with smooth walls. This is carried out at a low Reynolds number of $Re_\tau = 180$ to make use of the extensive DNS database of Vreman and Kuerten (2014). By validating at this Reynolds number we can determine suitable model and solver parameters without requiring extensive computing costs. Over the following year the model will be extended to a high Reynolds number to provide a base case for both comparisons against fish scale surfaces, and an estimation of the number of cells required.

6.2.1 Mathematical Model

Large eddy simulation is a technique used to study turbulence whereby the large turbulent structures are resolved and the small structures are modelled as a stress term. This is achieved by decomposing the velocity field into a filtered and residual term so that $U_i = \overline{U_i} + u_i'$. The filtered momentum (34) and continuity (35) equations (Pope, 2001) are defined as

$$\frac{\partial \overline{U}_i}{\partial t} + \frac{\partial \overline{U}_i \overline{U}_j}{\partial x_j} - \frac{\partial}{\partial x_j}(\overline{\sigma}_{ij} + \tau_{ij}) = -\frac{\partial \overline{P}}{\partial x_i}, \tag{34}$$

and

$$\frac{\partial \overline{U}_i}{\partial x_i} = 0, \tag{35}$$

where $\overline{\sigma}_{ij} = 2\nu \overline{S}_{ij}$ represents the resolved viscous stress tensor, $\overline{P} = \overline{p}/\rho$ is the resolved kinematic pressure, and $\overline{S}_{ij} = \frac{1}{2}\left(\frac{\partial \overline{U}_i}{\partial x_j} + \frac{\partial \overline{U}_j}{\partial x_i}\right)$ is the filtered rate of strain tensor. $\tau_{ij} = \overline{U}_i\overline{U}_j - \overline{U_i U_j}$ represents the effect of the unfiltered velocity field on the filtered field. This may be approximated using the model of Smagorinsky (1963):

$$\tau_{ij} - \frac{1}{3}\delta_{ij}\tau_{kk} = 2\nu_t \overline{S}_{ij}, \tag{36}$$

where ν_t is the sub-grid scale viscosity. Smagorinsky (1963) defines this sub-grid scale viscosity as

$$\nu_t = (C_s\Delta)^2 |\overline{S}|, \tag{37}$$

where C_s is the Smagorinsky constant and Δ is the filter width, based on the local grid size. The magnitude of the filtered rate of strain tensor is defined as $|\overline{S}| = (2\overline{S}_{ij}\overline{S}_{ij})^{1/2}$. The Smagorinsky model assumes a constant value of $C_s = 0.17$ (Smagorinsky, 1963). However, the assumption that C_s does not vary in space or time is a strong limitation to the model, as will be further discussed in section 6.2.3. An alternative method, first suggested by Germano et al. (1991), estimates the coefficient by filtering (34) and (35) a second time. By applying this filter we can define an addition stress term, equivalent to (36) just on a coarser grid of filter width $\widetilde{\Delta} = 2\Delta$: $T_{ij} - \frac{1}{3}\delta_{ij}T_{kk} = \widetilde{\overline{U}}_i\widetilde{\overline{U}}_j - \widetilde{\overline{U_iU_j}}$. By adopting the Germano identity (Germano et al., 1991), we relate the scales of motion between the two filter widths:

$$L_{ij} = T^r_{ij} - \widetilde{\tau}^r_{ij} = \widetilde{\overline{U}}_i\widetilde{\overline{U}}_j - \widetilde{\overline{U}_i\overline{U}_j}. \tag{38}$$

Unlike the equations for τ_{ij} and T_{ij}, equation 38 can be solved from the filtered velocity field. Assuming T_{ij} takes the same form as τ_{ij}, L_{ij} can be solved to find C_s:

$$L_{ij} = 2\Delta^2 \left[\widetilde{C_s^2|\overline{S}|\overline{S}_{ij}} - 4C_s^2|\widetilde{\overline{S}}|\widetilde{\overline{S}}_{ij} \right]. \tag{39}$$

This represents 5 equations with 1 unknown, the error of which is given by

$$e_{ij} = L_{ij} - M_{ij}C_s^2, \tag{40}$$

where

$$M_{ij} = 2\Delta^2 \left[\widetilde{|\overline{S}|\overline{S}_{ij}} - 4|\widetilde{\overline{S}}|\widetilde{\overline{S}}_{ij} \right].$$

It is assumed that the constant C_s does not vary spatially between the scales Δ and 2Δ, allowing it to be taken out of the filter term.

Typically the error is minimised by differentiating equation (40) with respect to C_s^2. However, this method requires both spatial averaging, in homogeneous directions, and clipping, in order to ensure C_s remains positive (energy dissipating). An alternative to this restrictive dynamic model is to average along particle paths using the model of Meneveau et al. (1996). In a Lagrangian frame of reference, the trajectory of a fluid particle for earlier times $t' < t$ is given by

$$\boldsymbol{z}(t') = \boldsymbol{x} - \int_{t'}^{t} \overline{\boldsymbol{u}}(\boldsymbol{z}(t''), t'')dt''. \tag{41}$$

In terms of the Lagrangian description the error to be minimised, (40), is

$$e_{ij}(\boldsymbol{z}, t') = L_{ij}(\boldsymbol{z}, t') - M_{ij}(\boldsymbol{z}, t')C_s^2(\boldsymbol{x}, t'), \tag{42}$$

where it is assumed that C_s can be removed from the filter by assuming it does not vary strongly over the scale of the test filter, an assumption that is investigated and justified by Meneveau et al. (1996). In order to minimise this error we define the total error as the pathline accumulation of the local error squared,

$$E = \int_{-\infty}^{t} e_{ij}(\mathbf{z}(t'), t') e_{ij}(\mathbf{z}(t'), t') W(t - t') dt', \tag{43}$$

where $W(t-t')$ is a weighting function, introduced in order to control the contributions from times closer to t. Differentiating with respect to C_s^2, and making use of (42), we obtain

$$C_s^2(\boldsymbol{x}, t) = \frac{f_{LM}}{f_{MM}}, \tag{44}$$

where

$$f_{LM} = \int_{-\infty}^{t} L_{ij} M_{ij}(\boldsymbol{z}(t'), t') W(t - t') dt', \tag{45}$$

and

$$f_{MM} = \int_{-\infty}^{t} M_{ij} M_{ij}(\boldsymbol{z}(t'), t') W(t - t') dt'. \tag{46}$$

A convenient choice of the weighting function is $W(t-t') = T^{-1} e^{-(t-t')/T}$ (Meneveau et al., 1996). This results in two transport equations for f_{LM} and f_{MM} rather than backward integrals in time:

$$\frac{Df_{LM}}{Dt} = \frac{1}{T}(L_{ij} M_{ij} - f_{LM}), \tag{47}$$

$$\frac{Df_{MM}}{Dt} = \frac{1}{T}(M_{ij} M_{ij} - f_{MM}). \tag{48}$$

T represents a timescale that controls the memory length. There are some natural choices for this parameter, highlighted by Meneveau et al. (1996), whereby the timescale can be controlled by the values of f_{LM} and f_{MM}. By taking $T = \theta \Delta (f_{LM} f_{MM})^{-1/8}$, where θ is a constant of order unity, the memory time will be reduced in both regions of high straining (high f_{MM}) and large nonlinear energy transfer (high f_{LM}). Typically $\theta = 1.5$ for most cases, although there is some solution dependence on this value. This dependency will be investigated in future work.

With these parameters now defined, the transport equations (47) and (48) can be solved and used to determine C_s. The turbulent stress tensor equation, (36), can now be solved, closing our set of equations.

6.2.2 Numerical Implementation

The equations are solved using OpenFOAM, a finite volume platform. The equations are discretised over a channel of dimensions $4.2\delta \times 2\delta \times 12.6\delta$ where δ is the channel half height. Similar dimensions are used by several authors such as Moser et al. (1999), and Vreman and Kuerten (2014) for a Reynolds number of $Re_\tau = 180$, although the influence of domain size on the turbulent statistics is still poorly understood (Vreman and Kuerten, 2014). Three simulations are presented in this report, one which which solves equations for only half the channel height and applies symmetry boundary conditions at the central plane, $y = \delta$. If validated, this model could reduce the number of required cells. The half channel simulation adopts a constant value of $C_s = 0.17$, validated against a full channel simulation using the same model. The final simulation adopts the dynamic Lagrangian model discussed in Section 6.2.1.

The mesh statistics are presented in Table 7. The total number of cells is $\sim 4M$, much fewer than an equivalent finite difference DNS of Vreman and Kuerten (2014) who used $\sim 33M$ grid points. A Cosine distribution is adopted in the wall-normal direction in order to capture the large gradients close to the wall. The y-normal boundary conditions can be observed from Table 8. The boundary conditions for f_{LM} and f_{MM} are defined by Meneveau et al. (1996). Periodic boundary conditions are applied in both streamwise and spanwise direction with a forcing term added to the momentum equation (34) in order to maintain a constant bulk Reynolds number in the z direction. The forcing term is derived by decomposing the pressure gradient into an average and fluctuating component; the average pressure gradient is adjusted each timestep in order to ensure a fixed mean velocity through the periodic faces, $\overline{\boldsymbol{U}}_{ave}$. A description of this technique is presented by Murthy and Mathur (1997).

A convenient choice for the parameters ν and $\overline{\boldsymbol{U}}_{ave}$ will fix the bulk Reynolds number to $Re_b = 2800$, corresponding to a shear Reynolds number of $Re_\tau \approx 180$. The choice of fixing the bulk flow Reynolds number is more natural when considering the validation of further results against experiments later this year. For a channel flow, Re_τ can be determined from the pressure gradient over the periodic boundary by applying a force balance over the domain:

$$Re_\tau = u_\tau \delta/\nu, \qquad u_\tau = \sqrt{\tau_w/\rho}, \qquad \tau_w/\rho = \delta \left.\frac{\partial P}{\partial z}\right|_{ave}.$$

A convenient choice of parameters are $\delta = 1$ and $\nu = 1/180$ resulting in an average shear velocity of $u_\tau \approx 1$ and $Re_\tau \approx 180$. The initial state makes use of a perturbation utility in OpenFOAM which adds instabilities to a flow profile of mean velocity $\overline{\boldsymbol{U}}_{ave}$. These instabilities grow between timesteps until a statistically steady and turbulent state is present.

The momentum (34), continuity (35), and the two Lagrangian transport equations (47) and (48) are discretised using second order schemes in both space and time. Backward Euler is adopted for discretisation in time and Gaussian integration in space. Linear

Table 7: Mesh statistics for the three LES cases. The half channel case takes $N_y = 64$

N_x	N_y	N_z	Δx^+	Δz^+	Δy^+_{min}	Δy^+_{max}
160	128	192	4.7	11.8	0.18	4.5

Table 8: Boundary conditions for the three LES cases.

		$y = 0$, $y = 2\delta$ (full channel)	$y = \delta$ (half channel)
	Variable	Condition	Condition
Half channel	U	Dirichlet	Neumann
	P	Neumann	Neumann
	ν_t	Neumann	Neumann
Full channel	U	Dirichlet	-
	P	Neumann	-
(Smagorinsky Model)	ν_t	Neumann	-
(Dynamic	f_{LM}	Dirichlet	-
Lagrangian Model)	f_{MM}	Neumann	-

interpolation is adopted in order to interpolate values from cell centres to cell faces. The PISO algorithm (Pressure-Implicit with Splitting of Operators) of Issa (1986) is adopted, whereby a pressure equation is derived from the momentum (34) and continuity equations (35). The PISO scheme operates using a two-step process: A predictor step and a corrector step. The semi-discrete form of (34) can be written as

$$\boldsymbol{C}\boldsymbol{u}^* = \boldsymbol{A}\boldsymbol{u}^* + \boldsymbol{H'}\boldsymbol{u}^* = \boldsymbol{r} - \nabla \boldsymbol{P}^n, \tag{49}$$

where $\boldsymbol{C}$ represents the implicit coefficient array, $\boldsymbol{u}^*$ is the predicted velocity, $\boldsymbol{r}$ is the explicit source terms and $\boldsymbol{P}^n$ represents the kinematic pressure at the previous time step. The matrix $\boldsymbol{C}$ can be split into diagonal and off diagonal components, $\boldsymbol{C} = \boldsymbol{A} + \boldsymbol{H'}$, and the linear equation (49) can be solved for $\boldsymbol{u}^*$. A Gauss-Seidel solver is adopted to solve this system, completing the predictor step. (49) can be manipulated in order to derive an equation to correct both the velocity and pressure from the predicted velocity:

$$\boldsymbol{A}\boldsymbol{u}^{**} + \boldsymbol{H'}\boldsymbol{u}^* = \boldsymbol{r} - \nabla \boldsymbol{P}^*, \tag{50}$$

$$\boldsymbol{u}^{**} = \boldsymbol{A}^{-1}\boldsymbol{H} - \boldsymbol{A}^{-1}\nabla \boldsymbol{P}^*, \tag{51}$$

where $\boldsymbol{H} = \boldsymbol{r} - \boldsymbol{H'}\boldsymbol{u}^*$. The inversion of $\boldsymbol{A}$ is trivial since it is symmetrical. By recognising that $\nabla \boldsymbol{u}^{**} = 0$, a Poisson equation for the corrected pressure can be derived:

$$\nabla^2(\boldsymbol{A}^{-1}\boldsymbol{P}^*) = \nabla \cdot (\boldsymbol{A}^{-1}\boldsymbol{H}). \tag{52}$$

This Laplacian equation is solved using a Geometric-algebraic multi-grid solver in order to update the pressure. The corrected velocity equation (51) is then solved to update the velocity. In order to ensure second order accuracy, (52) and (51) and solved twice, as recommended by Issa (1986). Equations (47) and (48) are discretised using the same method as the momentum equation and solved using a Gauss-Seidel solver. All equations are iteratively solved until a tolerance of 10^{-8} is met. An adaptive time-stepping scheme is adopted in order to ensure the Courant number does not exceed 0.5. Statistical averaging is carried out between the time intervals $t = 10\delta/u_\tau$ and $t = 40\delta/u_\tau$. This interval is much smaller than those adopted by Kim et al. (1987) and Vreman and Kuerten (2014), the impact of which will be discussed in Section 6.2.3.

Post-processing is carried out in MATLAB; Statistical quantities, such as means and standard deviations, are looped through each time-step directory and averaged in x and z. The results of which are compared to those of a spectral DNS code of Vreman and Kuerten (2014).

6.2.3 Results and Discussion

The calculated Reynolds numbers for the three simulations are compared against the DNS code in Table 9. All three simulations compute a slightly lower Reynolds number than the DNS, due to the method of calculating the forcing term. The target bulk Re was 2800, thus these small discrepancies are expected. The coefficients of friction match very well for both the half-channel and full-channel Smagorinsky models but the dynamic model underpredicts it by 1.11%. This will be further discussed when investigating variable profiles.

Little discrepancy can be observed from the velocity profiles of Figure 31. Small differences are present for the two Smagorinsky models in regions of high velocity gradient. Much larger differences are present in the root-mean-square (rms) statistics. Figure 32 indicates that the non-dynamic models underpredict the maximum values significantly in both the wall-normal and cross-stream directions. The near-wall gradients are also poorly captured by the non-dynamic models, suggesting that the models perform poorly in these regions. The half-channel simulation behaves similarly to the full-channel until getting close to $y = \delta$, at which point the solutions deviate significantly. This trend can be observed in many of the presented results (Figures 32 to 36) suggesting that the time dependent asymmetries in the flow have a large impact on the time averaged

Table 9: Comparison of global statistics between three LES cases and a DNS.

	Re_b	% to DNS	Re_τ	% to DNS	Re_c	% to DNS	C_f	% to DNS
DNS (Vreman and Kuerten, 2014)	2825	-	180	-	3290	-	0.00812	-
Half channel with Smagorinsky model	2794	-1.10	177.8	-1.22	3273	-0.52	0.00810	-0.25
Full channel with Smagorinsky model	2802	-0.81	178.5	-0.83	3269	-0.64	0.00817	0.62
Full channel with dynamic Lagrangian model	2800	-0.88	177.4	-1.44	3266	-0.73	0.00803	-1.11

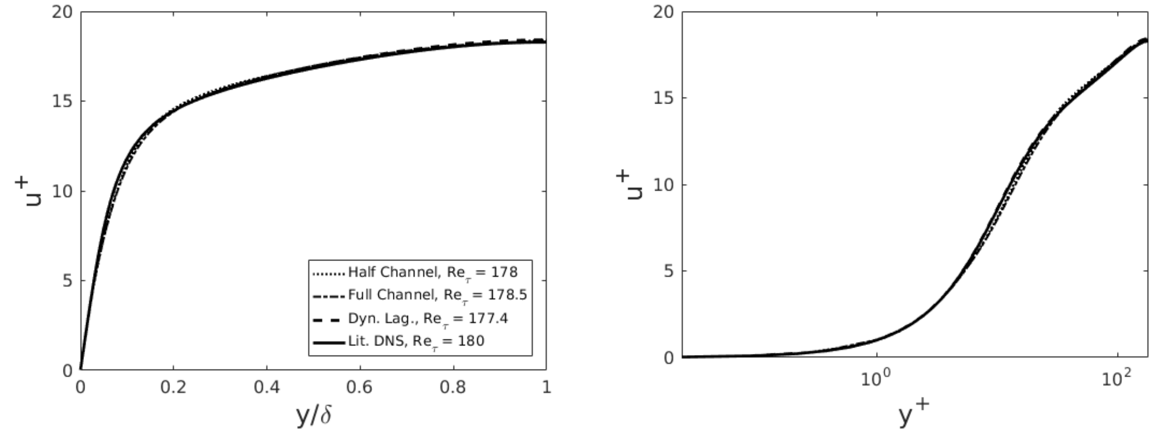

Figure 31: Comparison of mean velocity profiles for three LES cases and the DNS of Vreman and Kuerten (2014).

solution. The dynamic-Lagrangian model performs well, almost matching the DNS in all three directions. The small discrepancy in magnitude can be accounted for by the turbulent kinetic energy captured by the sub-grid scale stress term. The two full-channel rms velocity results collapse at $y = \delta$, suggesting that the dynamic Lagrangian model

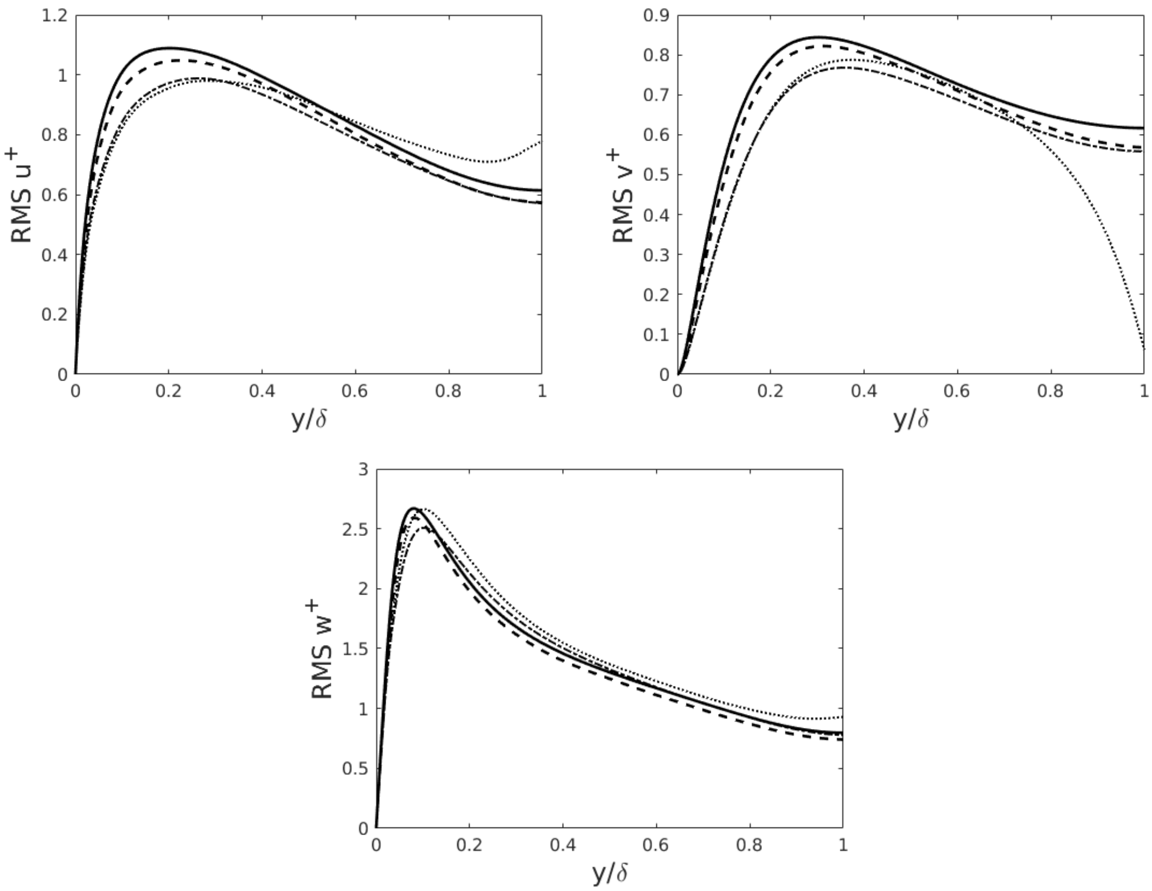

Figure 32: Comparison of root-mean-square velocity profiles for three LES cases and the DNS of Vreman and Kuerten (2014). For legend see Figure 31.

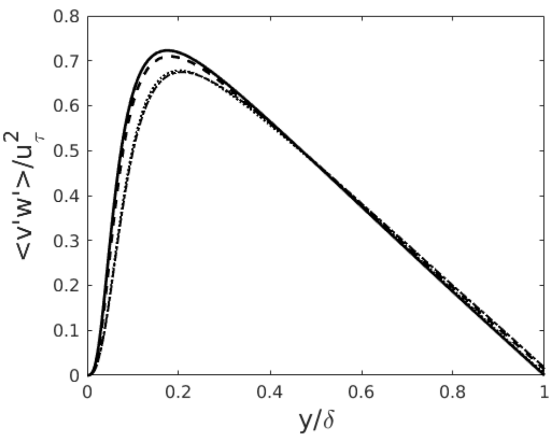

Figure 33: Comparison of Reynolds stresses for three LES cases and the DNS of Vreman and Kuerten (2014). For legend see Figure 31.

has little impact in regions far from the wall. The Reynolds stresses (Figure 33) are well predicted by the dynamic model but the maximum is under-predicted by the Smagorinsky model. A reasonable explanation for this is expressed by Pope (2001), who suggests that, for transitional flows, the fixed constant C_s must be reduced in order to predict the sub-grid scale stresses. Since the Reynolds number is low, this explanation seems reasonable.

The rms of vorticity profiles (Figure 34) similarly indicate that the dynamic model predicts the flow much better close to the wall. The non-dynamic models both significantly underpredict the vorticity fluctuations below $y^+ \approx 50$. Near the centre of the channel there is little difference between the two full-channel simulations, again suggesting that the dynamic modelling is most effective near the wall.

The skewness and flatness (kurtosis) of a variable q are defined as

$$S_q = \frac{\langle q^3 \rangle}{\langle q^2 \rangle^{3/2}}, \qquad F_q = \frac{\langle q^4 \rangle}{\langle q^2 \rangle^2}. \tag{53}$$

The skewness of velocity indicates the likelihood to take on large positive values (for $S_u > 0$) or large negative values (for $S_u < 0$). A high kurtosis suggests that large intermittent bursts in velocity are present in the flow, whilst a low kurtosis indicates that fluctuations are close to the mean value. The skewness profiles of Figure 35 suggest that the averaging time is too short to reach a unique solution, especially in the cross-stream direction. The small magnitudes of S_u suggest a symmetric probability distribution around the mean.

There is very poor agreement between the models for S_u suggesting that statistical convergence requires a much longer averaging period. The S_v profile indicates that all three models underpredict the magnitude of the maximum point, with the dynamic Lagrangian model performing worse than the Smagorinsky model. The streamwise skewness

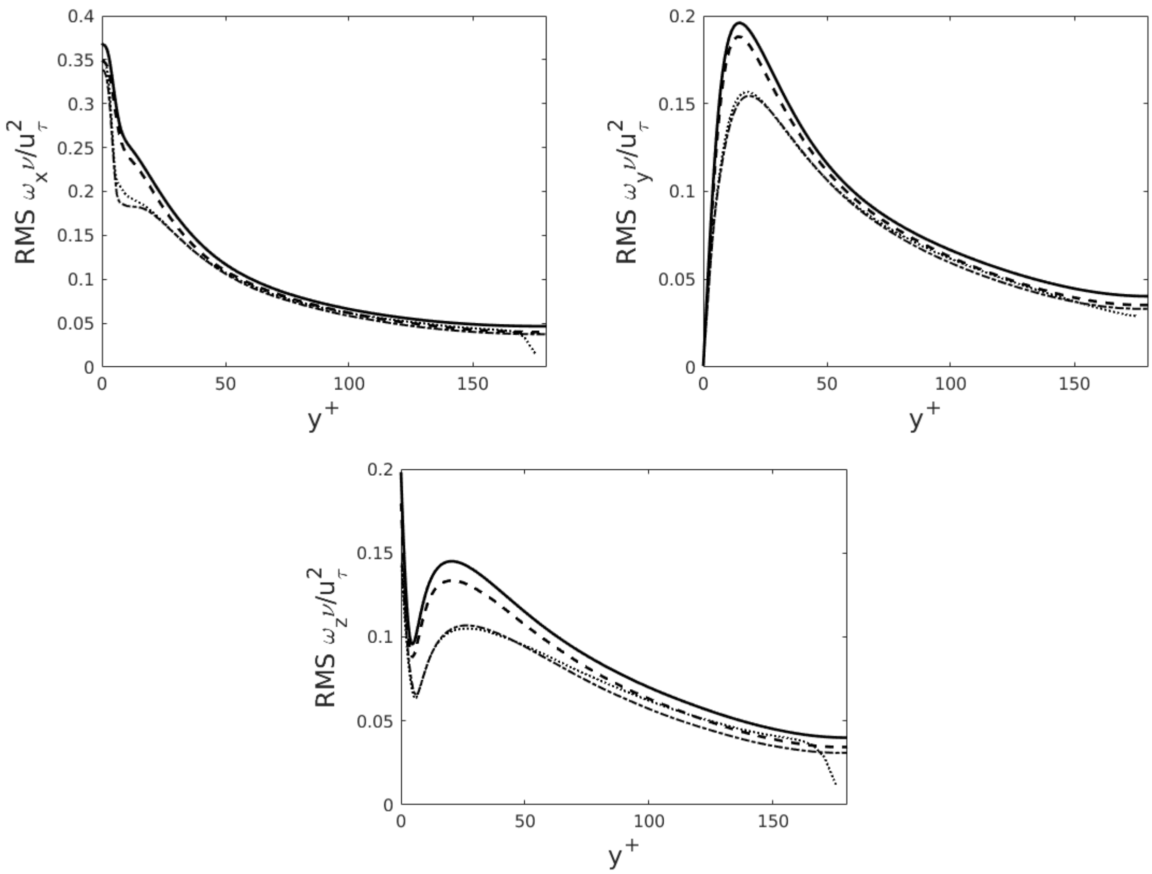

Figure 34: Comparison of RMS Vorticity for three LES cases and the DNS of Vreman and Kuerten (2014). For legend see Figure 31.

of velocity is better predicted by all three models but again the dynamic model performs worse. All three models underpredict the flatness of velocity at $y = 0$ (Figure 36). A possible reason for this is that events of large fluctuations are not captured over the period of averaging. In addition to this the number of cells close to the surface may not be sufficient in capturing these features. The general trends of the DNS results are followed for the two full-channel simulations. It is expected that these high order statistics require more temporal averaging than the other statistics presented.

6.2.4 Conclusions and Further Work

Three LES models have been assessed by their ability to predict an infinitely long and wide channel flow, validated against a DNS dataset (Vreman and Kuerten, 2014). Both the Smagorinsky model (Smagorinsky, 1963) and the dynamic Lagrangian model (Meneveau et al., 1996) predict the velocity profiles well, even for the simulation considering only half the channel. Deviations were more substantial when investigating RMS velocity, RMS vorticity, and Reynolds stresses. The half channel simulation fails to predict the flow close to the central channel due to restrictions on the flow. the Smagorinsky model generally underpredicts the magnitude of the fluctuations for all three components of vorticity, and

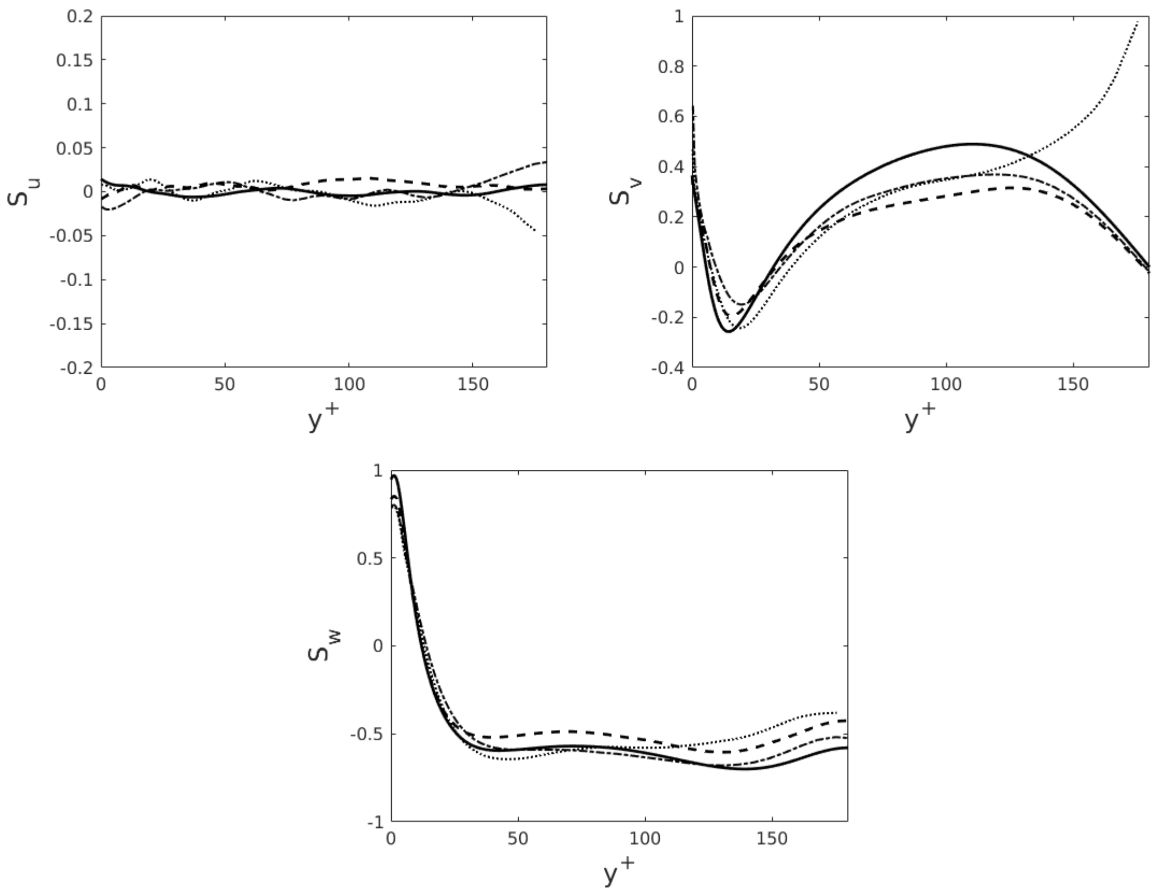

Figure 35: Comparison of skewness of velocity for three LES cases and the DNS of Vreman and Kuerten (2014). For legend see Figure 31.

the cross-stream and wall-normal fluctuations of velocity. The dynamic Lagrangian model compares well against the DNS for these statistics, accurately capturing the features close to the wall. However, the skewness and flatness of velocity are not well captured by the LES models. This is likely due to number of time steps that contribute to the statistics. Further work will investigate the sensitivity of these statistics to the temporal averaging.

In order to extend this work to shark scale surfaces the code will be run on generic polyhedral elements. Changes are likely to be made to the discretisation schemes in order to ensure stability, and changes will also have to be made to the post processing techniques. When validated, the code will be extended to shark scale surface.

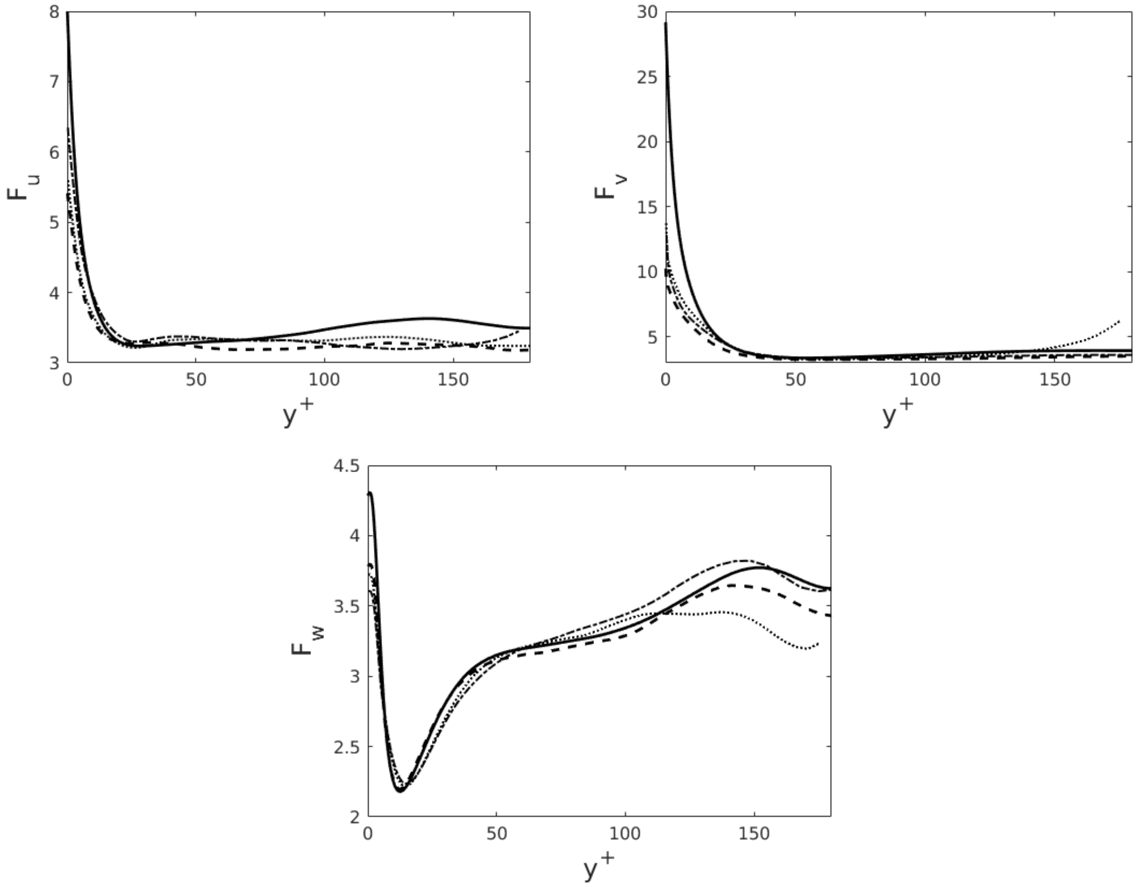

Figure 36: Comparison of flatness of velocity for three LES cases and the DNS of Vreman and Kuerten (2014). For legend see Figure 31.

7 6 Month Plan

The Gantt chart of Figure 37 indicates several different work packages, some of which are dependent on the completion of others. The experimental work is the main priority over the coming months since these results will form the first publication. The main risk associated with this work package is the 3D printing of the denticle arrays. There is potential to work in collaboration with the University of Nottingham who are currently printing samples of these scales. If the desired resolution can be met, then the arrays will be printed and the LDA experiments can commence.

The LES work package is also partly reliant on the 3D printing capabilities. The estimates of the scale size will be necessary if experiments are to match those of the numerics. However, there are other work packages that can be completed while the printing experiments are taking place. The experimental set up is also dependent on further CAD developments; since a full 500 mm by 100 mm array is unlikely to be printed in one section, the CAD model will have to be split. Care must be made in order to ensure the joints do not interfere with the surface. In addition to this, a new experimental plan must be developed in order to account for different grid sizes and sampling times.

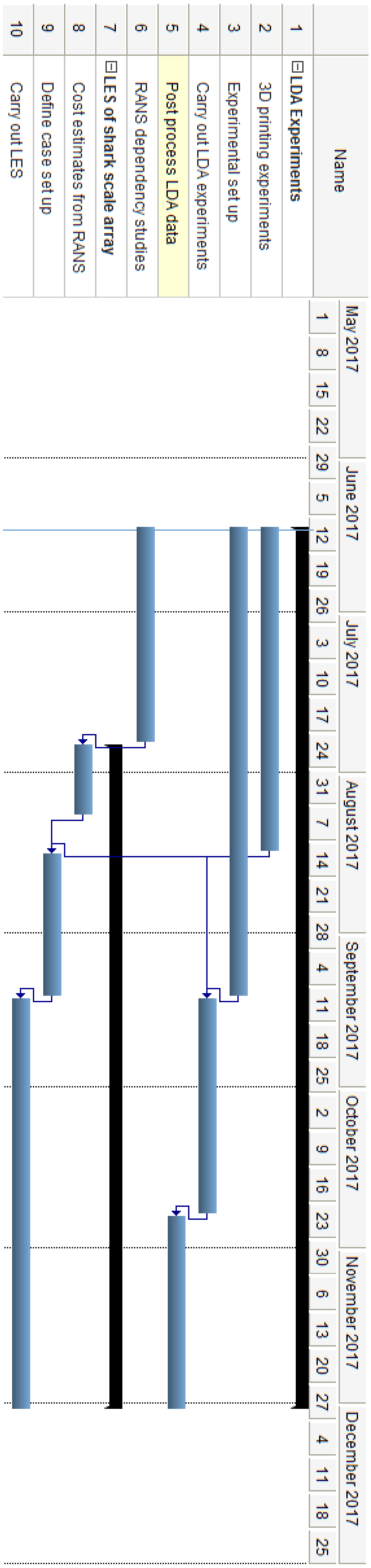

Figure 37: Gantt chart for the months June 2017 - Dec 2017.

RANS dependency studies also need further investigation, such as the dependencies on the turbulence closures, the number of scales in the periodic domain, and the discretisation schemes. The LES study is loosely dependent on the RANS studies since they provide an estimate to the required grid size.

8 High Level Plan

The main objectives of Section 4 are given the following timescales:

- Complete and write up LDA results for the flat plate flow over both smooth and two 3D printed shark scale surface (by Dec 2017).
- Carry out a LES for the same shark scales at a feasible scale width (to be defined by the RANS studies in Summer 2017), and compare findings against a flat plate LES, and a RANS model (by Mar 2018).
- If RANS methods can be validated then carry out a parametric analysis on the effect of shark scale geometry on the fluid flow (by July 2018).
- Carry out PIV and LES/RANS (depending on the validation of the models) for a separating flow, with and without scales (by March 2019).

9 Publications, conferences, and a long term placement

Four potential papers could be published if the above work packages can be completed:

1. An experimental investigation into the effects of smooth and ribletted sharkskin denticles on a flat plate boundary layer, using Laser Doppler Anemometry.
2. Large eddy simulation of smooth and ribletted sharkskin denticles in a tubulent channel flow.
3. A parametric study of the effects of sharkskin denticle geometry on a turbulent channel flow, using numerical methods.
4. An experimental investigation into the effects of sharkskin denticles on separating flows, using Particle Image Velocimetry.

There is potential for a placement with another UK university in order to carry out experiments on the flat plates with force balances. These results would complement the findings of the LDA experiments, but would not be essential for publication.

There are several journals that could be approached with these papers:

- Bioinspiration & Biomimetics,
- Experiments in Fluids,
- Journal of Fluid Mechanics,
- Physics of Fluids.

A list of potential conferences is presented below:

- ICATDL 2018 : 20th International Conference on Aerodynamics, Thrust, Drag and Lift (Paris, May 2018),
- ECCM - ECFD 2018 - European conference for computational fluid dynamics (Glasgow, June 2018),
- Lisbon 2018 international symposium on applications of laser and imaging techniques to fluid mechanics (Lisbon, July 2018).

References

Bechert, D., Bruse, M., and Hage, W. (2000). Experiments with three-dimensional riblets as an idealized model of shark skin. *Experiments in fluids*, 28(5):403–412.

Bechert, D., Bruse, M., Hage, W., Van der Hoeven, J. T., and Hoppe, G. (1997). Experiments on drag-reducing surfaces and their optimization with an adjustable geometry. *Journal of fluid mechanics*, 338:59–87.

Bechert, D., Hoppe, G., and Reif, W.-E. (1985). On the drag reduction of the shark skin. In *1985 AIAA Shear Flow Control Conference*.

Bixler, G. D. and Bhushan, B. (2013). Fluid drag reduction with shark-skin riblet inspired microstructured surfaces. *Advanced Functional Materials*, 23(36):4507–4528.

Boomsma, A. (2015). *Drag Reduction by Riblets & Sharkskin Denticles: A Numerical Study*. PhD thesis, UNIVERSITY OF MINNESOTA.

Boomsma, A. and Sotiropoulos, F. (2016). Direct numerical simulation of sharkskin denticles in turbulent channel flow. *Physics of Fluids (1994-present)*, 28(3):035106.

Büttner, C. C. and Schulz, U. (2011). Shark skin inspired riblet structures as aerodynamically optimized high temperature coatings for blades of aeroengines. *Smart Materials and Structures*, 20(9):094016.

Caram, J. and Ahmed, A. (1991). Effect of riblets on turbulence in the wake of an airfoil. *AIAA journal*, 29(11):1769–1770.

Caretto, L., Gosman, A., Patankar, S., and Spalding, D. (1973). Two calculation procedures for steady, three-dimensional flows with recirculation. In *Proceedings of the third international conference on numerical methods in fluid mechanics*, pages 60–68. Springer.

Chamorro, L. P., Arndt, R., and Sotiropoulos, F. (2013). Drag reduction of large wind turbine blades through riblets: Evaluation of riblet geometry and application strategies. *Renewable energy*, 50:1095–1105.

Chen, H., Zhang, X., Ma, L., Che, D., Zhang, D., and Sudarshan, T. (2014). Investigation on large-area fabrication of vivid shark skin with superior surface functions. *Applied Surface Science*, 316:124–131.

Choi, K.-S. (1990). Effects of longitudinal pressure gradients on turbulent drag reduction with riblets. In *Turbulence Control by Passive Means*, pages 109–121. Springer.

Chu, D. C. and Karniadakis, G. E. (1993). A direct numerical simulation of laminar and turbulent flow over riblet-mounted surfaces. *Journal of Fluid Mechanics*, 250:1–42.

Clauser, F. H. (1956). The turbulent boundary layer. *Advances in applied mechanics*, 4:1–51.

Coustols, E. and Schmitt, V. (1990). Synthesis of experimental riblet studies in transonic conditions. In *Turbulence Control by Passive Means*, pages 123–140. Springer.

Dean, B. and Bhushan, B. (2010). Shark-skin surfaces for fluid-drag reduction in turbulent flow: a review. *Philosophical Transactions of the Royal Society of London A: Mathematical, Physical and Engineering Sciences*, 368(1929):4775–4806.

Debisschop, J. and Nieuwstadt, F. (1996). Turbulent boundary layer in an adverse pressure gradient-effectiveness of riblets. *AIAA journal*, 34(5):932–937.

Díez, G., Soto, M., and Blanco, J. (2015). Biological characterization of the skin of shortfin mako shark isurus oxyrinchus and preliminary study of the hydrodynamic behaviour through computational fluid dynamics. *Journal of fish biology*, 87(1):123–137.

Flack, K. A. and Schultz, M. P. (2010). Review of hydraulic roughness scales in the fully rough regime. *Journal of Fluids Engineering*, 132(4):041203.

Fletcher, T., Altringham, J., Peakall, J., Wignall, P., and Dorrell, R. (2014). Hydrodynamics of fossil fishes. In *Proc. R. Soc. B*, volume 281, page 20140703. The Royal Society.

Fletcher, T. M. (2015). *The Evolution of Speed: an empirical and comparative analysis of drag-reducing scales in early fishes.* PhD thesis, University of Leeds.

Fukagata, K., Iwamoto, K., and Kasagi, N. (2002). Contribution of reynolds stress distribution to the skin friction in wall-bounded flows. *Physics of Fluids*, 14(11):L73–L76.

García-Mayoral, R. and Jiménez, J. (2011). Drag reduction by riblets. *Philosophical Transactions of the Royal Society of London A: Mathematical, Physical and Engineering Sciences*, 369(1940):1412–1427.

Garcia-Mayoral, R. and Jimenez, J. (2011). Hydrodynamic stability and breakdown of the viscous regime over riblets. *Journal of Fluid Mechanics*, 678:317–347.

García-Mayoral, R. and Jiménez, J. (2012). Scaling of turbulent structures in riblet channels up to re τ 550. *Physics of Fluids*, 24(10):105101.

Germano, M., Piomelli, U., Moin, P., and Cabot, W. H. (1991). A dynamic subgrid-scale eddy viscosity model. *Physics of Fluids A: Fluid Dynamics (1989-1993)*, 3(7):1760–1765.

Goring, D. G. and Nikora, V. I. (2002). Despiking acoustic doppler velocimeter data. *Journal of Hydraulic Engineering*, 128(1):117–126.

Grüneberger, R. and Hage, W. (2011). Drag characteristics of longitudinal and transverse riblets at low dimensionless spacings. *Experiments in Fluids*, 50(2):363–373.

Han, M., Lim, H. C., Jang, Y.-G., Lee, S. S., and Lee, S.-J. (2003). Fabrication of a micro-riblet film and drag reduction effects on curved objects. In *TRANSDUCERS, Solid-State Sensors, Actuators and Microsystems, 12th International Conference on, 2003*, volume 1, pages 396–399. IEEE.

Issa, R. I. (1986). Solution of the implicitly discretised fluid flow equations by operator-splitting. *Journal of computational physics*, 62(1):40–65.

Jimenez, J. (2004). Turbulent flows over rough walls. *Annu. Rev. Fluid Mech.*, 36:173–196.

Kasagi, N. and Fukagata, K. (2006). *The FIK identity and its implication for turbulent skin friction control*. World Scientific, Singapore.

Kim, J., Moin, P., and Moser, R. (1987). Turbulence statistics in fully developed channel flow at low reynolds number. *Journal of fluid mechanics*, 177:133–166.

Klumpp, S., Guldner, T., Meinke, M., and Schröder, W. (2010). Riblets in a turbulent adverse-pressure gradient boundary layer. In *5th Flow Control Conference*, page 4706.

Lang, A. W., Bradshaw, M. T., Smith, J. A., Wheelus, J. N., Motta, P. J., Habegger, M. L., and Hueter, R. E. (2014). Movable shark scales act as a passive dynamic micro-roughness to control flow separation. *Bioinspiration & biomimetics*, 9(3):036017.

Lee, S.-J. and Lee, S.-H. (2001). Flow field analysis of a turbulent boundary layer over a riblet surface. *Experiments in fluids*, 30(2):153–166.

Luchini, P., Manzo, F., and Pozzi, A. (1991). Resistance of a grooved surface to parallel flow and cross-flow. *Journal of fluid mechanics*, 228:87–109.

Luo, Y., Liu, Y., Anderson, J., Li, X., and Li, Y. (2015a). Improvement of water-repellent and hydrodynamic drag reduction properties on bio-inspired surface and exploring sharkskin effect mechanism. *Applied Physics A*, 120(1):369–377.

Luo, Y., Wang, J., Sun, G., Li, X., and Liu, Y. (2015b). Experimental investigations on manufacturing different-shaped bio-inspired drag-reducing morphologies and hydrodynamic testing. *Experimental Techniques*.

Meneveau, C., Lund, T. S., and Cabot, W. H. (1996). A lagrangian dynamic subgrid-scale model of turbulence. *Journal of Fluid Mechanics*, 319:353–385.

Menter, F., Kuntz, M., and Langtry, R. (2003). Ten years of industrial experience with the sst turbulence model. *Turbulence, heat and mass transfer*, 4(1):625–632.

Menter, F. R. (1994). Two-equation eddy-viscosity turbulence models for engineering applications. *AIAA journal*, 32(8):1598–1605.

Moser, R. D., Kim, J., and Mansour, N. N. (1999). Direct numerical simulation of turbulent channel flow up to re= 590. *Phys. Fluids*, 11(4):943–945.

Murthy, J. and Mathur, S. (1997). Periodic flow and heat transfer using unstructured meshes. *International journal for numerical methods in fluids*, 25(6):659–677.

Neumann, D. and Dinkelacker, A. (1991). Drag measurements on v-grooved surfaces on a body of revolution in axial flow. *Applied Scientific Research*, 48(1):105–114.

Newhall, K. A. (2006). *Turbulent boundary layers: a look at skin friction, pressure gradient, surface roughness and the power law*. PhD thesis, Rensselaer Polytechnic Institute.

Nieuwstadt, F., Wolthers, W., Leijdens, H., Krishna Prasad, K., and Schwarz-van Manen, A. (1993). The reduction of skin friction by riblets under the influence of an adverse pressure gradient. *Experiments in fluids*, 15(1):17–26.

Nikuradse, J. (1933). Laws of flow in rough pipes. In *VDI Forschungsheft*. Citeseer.

Perlin, M., Dowling, D. R., and Ceccio, S. L. (2016). Freeman scholar review: Passive and active skin-friction drag reduction in turbulent boundary layers. *Journal of Fluids Engineering*, 138(9):091104.

Pope, S. B. (2001). Turbulent flows.

Reidy, L. W. and Anderson, G. W. (1988). Drag reduction for external and internal boundary layers using riblets and polymers. *AIAA Pap*, (88-0138).

Reif, W.-E. (1985). *Squamation and ecology of sharks*. Senckenbergische Naturforschende Gesellschaft.

Rohr, J., Andersen, G., Reidy, L., and Hendricks, E. (1992). A comparison of the drag-reducing benefits of riblets in internal and external flows. *Experiments in fluids*, 13(6):361–368.

Sareen, A., Deters, R., Henry, S., and Selig, M. (2011). Paper# aiaa-2011-558. In *49th AIAA Aerospace Sciences Meeting, AIAA, Orlando, FL, New York*.

Smagorinsky, J. (1963). General circulation experiments with the primitive equations: I. the basic experiment*. *Monthly weather review*, 91(3):99–164.

Subaschandar, N., Kumar, R., and Sundaram, S. (1999). Drag reduction due to riblets on a gaw (2) airfoil. *Journal of aircraft*, 36(5):890–892.

Sundaram, S., Viswanath, P., and Rudrakumar, S. (1996). Viscous drag reduction using riblets on naca 0012 airfoil to moderate incidence. *AIAA journal*, 34(4):676–682.

Sundaram, S., Viswanath, P., and Subaschandar, N. (1999). Viscous drag reduction using riblets on a swept wing. *AIAA journal*, 37(7):851–856.

Viswanath, P. and Mukund, R. (1995). Turbulent drag reduction using riblets on a supercritical airfoil at transonic speeds. *AIAA journal*, 33(5):945–947.

Vreman, A. and Kuerten, J. (2014). Comparison of direct numerical simulation databases of turbulent channel flow at reτ= 180. *Physics of Fluids (1994-present)*, 26(1):015102.

Walsh, M. J. (1982). Turbulent boundary layer drag reduction using riblets. In *AIAA, Aerospace sciences meeting*, volume 1.

Walsh, M. J. (1990). Effect of detailed surface geometry on riblet drag reduction performance. *Journal of Aircraft*, 27(6):572–573.

Wen, L., Weaver, J. C., and Lauder, G. V. (2014). Biomimetic shark skin: design, fabrication and hydrodynamic function. *Journal of Experimental Biology*, 217(10):1656–1666.

Wen, L., Weaver, J. C., Thornycroft, P. J., and Lauder, G. V. (2015). Hydrodynamic function of biomimetic shark skin: effect of denticle pattern and spacing. *Bioinspiration & Biomimetics*, 10(6):066010.

Wetzel, K. K. and Farokhi, S. (1996). Interaction of riblets and votex generators on an airfoil.

Wilkinson, S. and Lazos, B. (1988). Direct drag and hot-wire measurements on thin-element riblet arrays. In *Turbulence Management and Relaminarisation*, pages 121–131. Springer.

Yang, S.-Q., Li, S., Tian, H.-P., Wang, Q.-Y., and Jiang, N. (2016). Tomographic piv investigation on coherent vortex structures over shark-skin-inspired drag-reducing riblets. *Acta Mechanica Sinica*, 32(2):284–294.

Zhang, D., Li, Y., Han, X., Li, X., and Chen, H. (2011a). High-precision bio-replication of synthetic drag reduction shark skin. *Chinese Science Bulletin*, 56(9):938–944.

Zhang, D.-Y., Luo, Y.-H., Xiang, L., and Chen, H.-W. (2011b). Numerical simulation and experimental study of drag-reducing surface of a real shark skin. *Journal of Hydrodynamics, Ser. B*, 23(2):204–211.

Zhang, Z. (2010). Lda application examples. In *LDA Application Methods*. Springer.

Zhao, D.-Y., Huang, Z.-P., Wang, M.-J., Wang, T., and Jin, Y. (2012). Vacuum casting replication of micro-riblets on shark skin for drag-reducing applications. *Journal of Materials Processing Technology*, 212(1):198–202.